NASA Contractor Report 186026

Flight Validation of a Pulsed Smoke Flow Visualization System

Donald T. Ward and Kenneth M. Dorsett

Contract NCC 2-742
September 1993

National Aeronautics and
Space Administration

NASA Contractor Report 186026

Flight Validation of a Pulsed Smoke Flow Visualization System

Donald T. Ward and Kenneth M. Dorsett
Texas A & M University
College Station, Texas

Prepared for
Dryden Flight Research Facility
Edwards, California
Under Contract NCC 2-742

1993

National Aeronautics and
Space Administration

Dryden Flight Research Facility
Edwards, California 93523-0273

ABSTRACT

A flow visualization scheme, designed to measure vortex fluid dynamics on research aircraft, was validated in flight. Strake vortex trajectories and axial core velocities were determined using pulsed smoke, high-speed video images, and semiautomated image edge detection hardware and software. Smoke was pulsed by using a fast-acting three-way valve. After being redesigned because of repeatedly jamming in flight, the valve shuttle operated flawlessly during the last two tests. A 25-percent scale, Gothic strake was used to generate vortex over the wing of a GA-7 Cougar and was operated at a local angle of attack of 22° and Reynolds number of approximately 7.8×10^5/ft. Maximum axial velocities measured in the vortex core were between 1.75 and 1.95 times the freestream velocity. Analysis of the pulsed smoke system's affect on forebody vortices indicates that the system may reorient the forebody vortex system; however, blowing momentum coefficients normally used will have no appreciable affect on the leading-edge extension vortex system. It is recommended that a similar pulsed smoke system be installed on the F/A-18 High Angle Research Vehicle and that this approach be used to analyze vortex core dynamics during the remainder of its high-angle-of-attack research flights.

TABLE OF CONTENTS

LIST OF TABLES

LIST OF FIGURES

LIST OF SYMBOLS AND ACRONYMS

Symbol	Name	Dimensions
AOA, α	Angle of Attack	degrees
AOS, β	Angle of Sideslip	degrees
b	Span	ft
c	Chord	ft
C_n	Yawing Moment Coefficient	(-)
C_Y	Side Force Coefficient	(-)
C_μ	Blowing Momentum Coefficient	(-)
i	Incidence Angle	degrees
l_i	Symmetric Distortion Parameter	(-)
p_i	Asymmetric Distortion Parameter	(-)
r	Focal Plane Radial Distance	inches
R_N, R_e	Reynolds Number	(-)
S	Reference Area	sq. ft
t	Time	seconds
V	Velocity	ft/sec
x_o	Focal Plane Principal Point X Offset	inches
y_o	Focal Plane Principal Point Y Offset	inches
x	Focal Plane X Coordinate	inches
y	Focal Plane Y Coordinate	inches
X	X Station Location	inches
Y	Y Station Location	inches
Z	Z Station Location	inches
Λ_{LE}	Leading Edge Sweep	degrees

Subscript	Description
∞	Freestream
core	Core
mac	Mean Aerodynamic Chord
r	Root
s	Strake
w	Wing

Acronym	Description
CCD	Charge Coupled Device
FOV	Field of View
frps	Frames per Second
HARV	High Angle of Attack Research Vehicle
ISFVS	Intermittent Smoke Flow Visualization System
KIAS	Knots Indicated Airspeed
LDV	Laser Doppler Velocimetry
LOS	Line of Sight
VAC	Video Analog Collection
VTR	Video Tape Recorder
2-D	Two-Dimensional
3-D	Three-Dimensional

INTRODUCTION AND BACKGROUND

An intermittent (pulsed smoke flow visualization system (ISFVS) has been developed and tested at Texas A&M University. Flight testing of this system was completed under NCC 2-742 with NASA Ames-Dryden Flight Research Facility, Edwards, California.

The ISFVS consists of a canister containing an electrically ignited chemical smoke grenade, a plenum chamber, and a three-way valve[1]. When fired, the smoke cartridge burns a mixture of sugar, potassium chlorate, and terephthalic acid. The terephthalic acid is vaporized into a gas, and exhausted through the plenum chamber and out the valve. The valve can be used to either block or divert the smoke flow to an alternate port, thus creating individual "packets" of smoke. To protect against potentially hazardous over-pressure conditions, a 0.002 inch brass shim rupture disk was provided in the cartridge canister to preclude catastrophic failure of the system. The rupture disk was designed to fail between 50 and 70 psid. Myatt and Ward[1,2] discuss the detailed design of the ISFVS.

The ISFVS was developed for the F/A-18 High Angle of Attack Research Vehicle (HARV) to collect quantitative flow visualization data of vortex behavior at high angles of attack (AOA). With the development of three-dimensional (3-D) video imaging systems, time-matched video images from multiple cameras can be used to reconstruct the 3-D trajectory of a vortex core. Furthermore, by chopping the smoke into individual packets, the axial velocity within the vortex core can be obtained by numerically differentiating the video derived trajectories[3].

In the first phase of the project, the system was built and ground tested. A prediction code was written in FORTRAN to thermodynamically model the system such that pressures, temperatures and smoke exit velocities could be simulated for various conditions. The code was satisfactorily validated using experimental data collected by ground firing the ISFVS[1,2].

A commercially available video imaging system was used to digitize and analyze video images of a strake-generated vortex core. The system can record video data simultaneously from up to four cameras with frame rates as high as 200 frames per second (frps). The data are digitized and stored as numerical information to be analyzed using system software.

Wind tunnel and flight tests were conducted using the ISFVS to determine its usefulness in collecting video derived three dimensional vortex trajectory and velocity data. The video imaging system was utilized to collect and numerically analyze the video data.

Description of Video Imaging Equipment

The video imaging hardware consisted of a four channel video processor, two video cameras, three 200 frps video tape recorders (VTRs), and a 13" monochrome monitor. The software was supported on a graphics work station.

The video processor controlled the cameras, and digitized the video data. It detected (based on levels of contrast) the edges of images and digitized the screen positions into files which were then transmitted to the work station for analysis.

The cameras were multi-speed CCTV video cameras mounting 7mm C-mount lenses. The cameras were operated at their maximum speed of 200 frps.

The video analysis software consisted of modules that were used to control collection of the video data, manually edit the images, compute image centroids and paths, and plot various data.

WIND TUNNEL TEST

The ISFVS was tested in the TAMU 7' x 10' low speed wind tunnel. The purpose of the test was to determine whether the individual smoke packets maintained their sharp leading edges when injected into a vortex core at near flight dynamic pressures. The following sections describe the ISFVS wind tunnel test.

Test Description

The test was conducted at a freestream velocity of 100 ft/sec and a Reynolds number of 5.73 x 10^5 per foot. Figure 1 illustrates the wind tunnel apparatus.

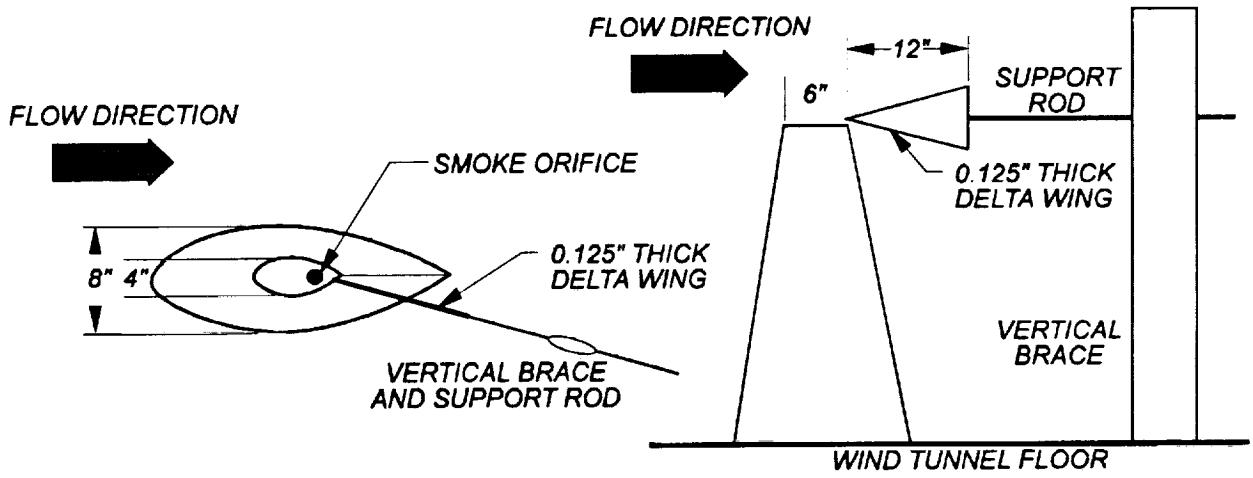

a: Top View **b: Side View**

Figure 1: Wind Tunnel Apparatus

A sharply swept delta wing (76° leading edge sweep) was inclined in the flow at 30° AOA. Smoke was injected into the flow near the apex of the delta planform. Three different plenum volumes, as well as various valve sequences were tested to determine their effects upon smoke quality and chamber pressure. The system was tested with the valve diverting as well as blocking the flow. Valve timing was critical only for the blocked flow mode, since an over pressure condition in the system could result. Otherwise, valve timing was based upon the desired number

of targets visible to the cameras at any given time. The valve controller was the same as the one described by Ward and Myatt[2].

The video system was set up around the test section using two video cameras. The cameras were positioned so their lines of sight were nearly orthogonal to improve the accuracy of the regression routines used to determine the 3-D trajectories. Figure 2 is a schematic of the video imaging system used during the wind tunnel test.

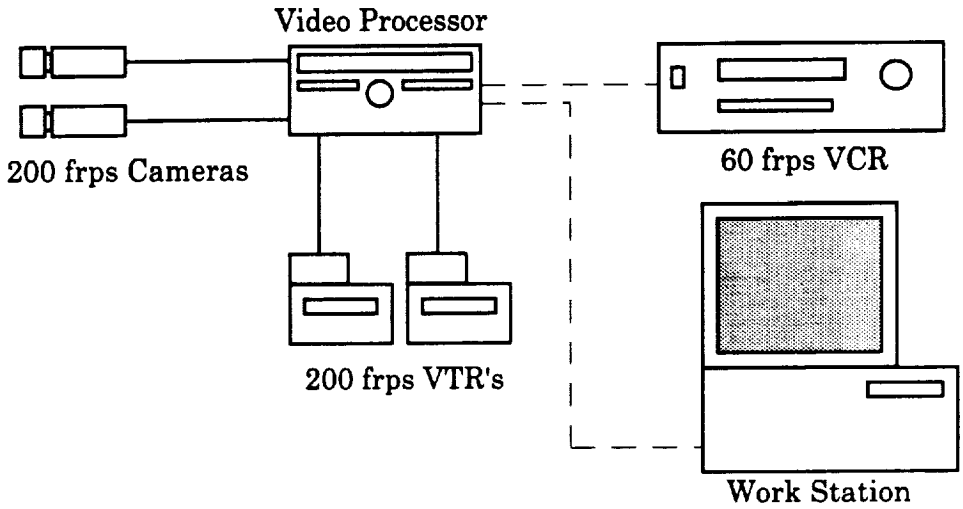

Figure 2: Semi-Automated Data System

Cartridge chamber and plenum temperatures were recorded along with plenum pressure. These values were used for additional comparison with predictions and previously collected data. Table 1 lists the conditions for each run.

Table 1: Summary of Wind Tunnel Test Parameters

Run No.	Plenum Size	Valve Mode
1	Large	Diverting*
2	Large	Diverting
3	Large	Blocking
4	Medium	Blocking
5	Small	Blocking

*First run repeated due to data collection problems
Large = 175.7 in^3
Medium = 125.7 in^3
Small = 100.7 in^3

Wind Tunnel Test Results

A total of five cartridges were fired during the test. During the final run, the rupture disk blew out as a result of too long a dwell time for the small plenum

volume. The large plenum volume allowed the greatest variation of valve dwell times.

Varying the plenum volumes had no noticeable effect on the quality of smoke produced. Higher peak plenum pressures were realized when operating with the smaller plenum volumes.

The video cameras were not fast enough to obtain the quality of data desired. For most of the runs, only five to eight frames of data were obtained for each smoke puff. Therefore, only rudimentary trends of the velocity profiles could be obtained. Furthermore, while the leading edges of each smoke puff remained fairly cohesive and distinct, the smoke completely enveloped the small delta wing used as the vortex generator. The wing leading edge vortex cores were never adequately defined by the smoke. A larger model would have been desirable, although the data were adequate to show that the method of data collection was feasible. Similar problems were encountered by Morris[3] and Nelson[4]. Figure 3 depicts a typical video frame taken from the top camera during the test.

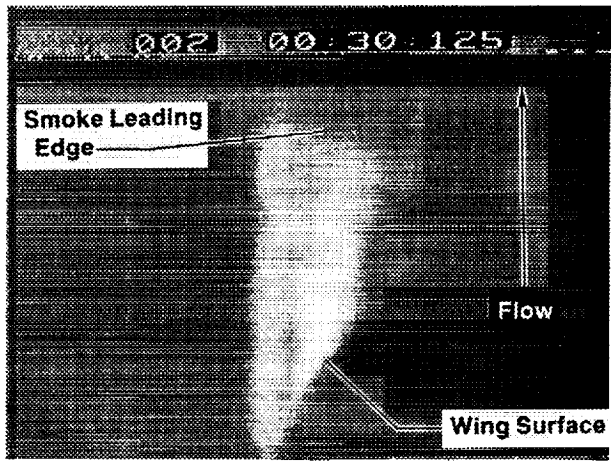

Figure 3: View of Test Section From Top Camera

Figure 4 shows vortex core trajectory profiles taken from numerous smoke puffs. Comparisons made between these data and video frames indicate that the video imaging system faithfully reproduced the trajectory of the smoke in the wake of the wing.

Figure 5 illustrates the axial velocity profile with respect to axial direction (X). Axial velocity was determined by taking the Euclidean norm of X, Y and Z component velocities. The velocities were non-dimensionalized by dividing by freestream velocity; 100 ft/sec in this case. A considerable amount of scatter exists in these data. However, the results were repeatable from run to run. The least squares polynomial curves for the velocity ratios all lay in the region between 0.6 and 0.8.

Because the delta wing leading edge vortices were not adequately seeded during the wind tunnel test, the velocity data presented in Figure 5 are relatively meaningless. It is impossible to compare these data with other published data.

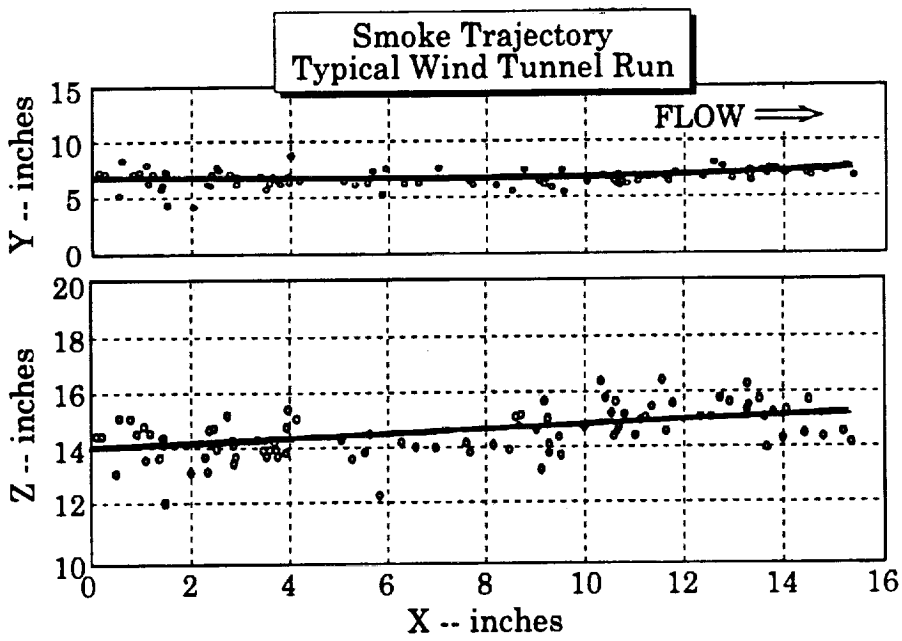

Figure 4: Video Derived Smoke Trajectories

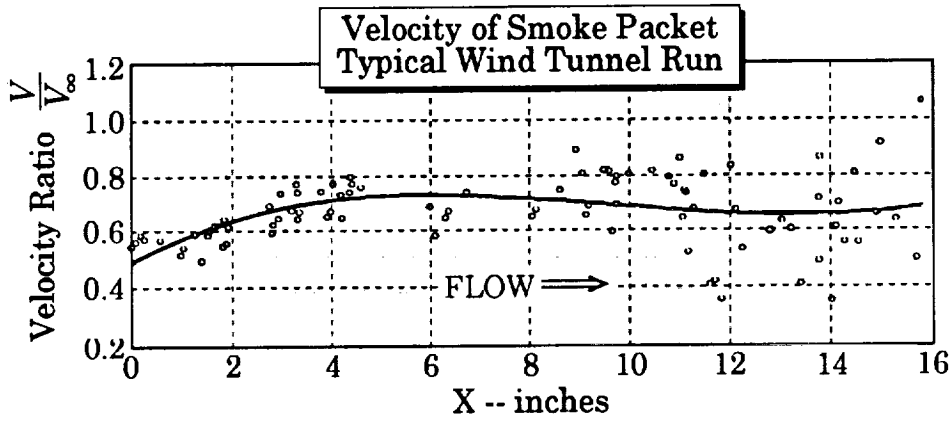

Figure 5: Typical Velocity Data Obtained During Wind Tunnel Test

FLIGHT VALIDATION

Following the wind tunnel test, a flight test program was begun to gain experience with the ISFVS in flight. The primary objective of the flight test program was to demonstrate the usefulness of the ISFVS in obtaining accurate trajectory and velocity measurements of a LEX vortex in flight. Secondary objectives were to provide a full-scale shake-down of the system while looking at camera calibration and location, potential data collection problems, flight safety, and system reliability. The following sections summarize the lessons learned using the ISFVS in flight.

Description of Aircraft Modifications

A Grumman American GA-7 Cougar was used as the ISFVS test bed. This aircraft is a light twin general aviation airplane owned and operated by the TAMU Flight Mechanics Laboratory. The Cougar had been used as a test bed for various past research projects, and as a result had some unique modifications that made it ideal for the ISFVS tests. Figure 6 is a three-view sketch of this test airplane[5].

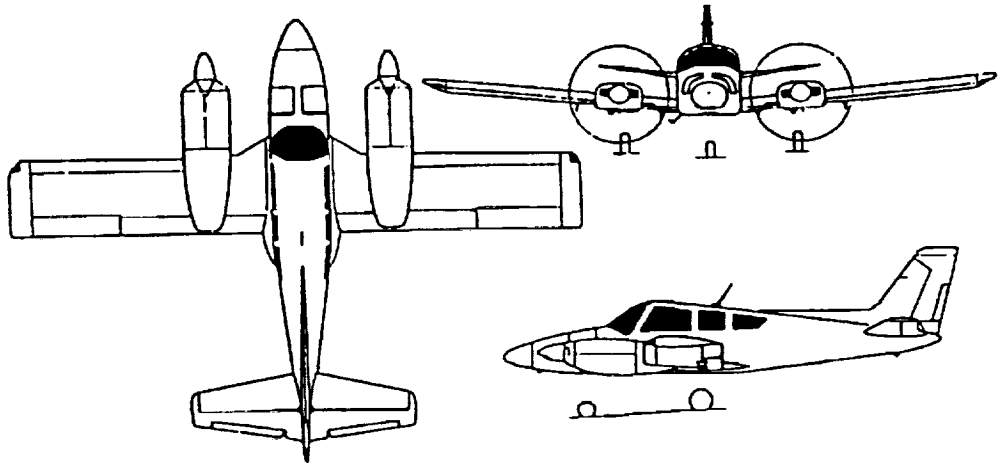

Figure 6: GA-7 Cougar Three-View[5]

An avionics equipment rack had been built into the passenger compartment of the Cougar for use during an earlier project. Due to the amount of equipment that needed to be carried aloft during the ISFVS tests, the existence of the rack saved considerable time and expense to the test program. In this case the rack carried the following equipment: video processor; computer and color monitor; two video camera power supplies; ISFVS valve control hardware; two 200 frps video tape recorders (VTR), control boxes and power supplies; three 500 watt power inverters; black and white video monitor. The copilot's seat was turned facing aft such that the flight test engineer could operate the work station in flight.

A 16 channel analog to digital (A/D) conversion board was used as an interface between the computer and the system hardware. Valve control, cartridge ignition, and ISFVS pressure and temperature data collection were controlled using four A/D and two D/A channels. Data were sampled at 1000 Hz for 60 seconds during the cartridge burn. The ISFVS included thermocouple ports so that cartridge chamber, plenum, valve inlet and valve exit temperature could be measured using Type J shielded thermocouples. Additionally, plenum pressure was recorded using a 50 psid pressure transducer. Figure 7 illustrates the data collection equipment.

The aircraft electrical system was modified by replacing the existing 60 amp alternator in the right nacelle with a 90 amp alternator. This modification provided sufficient electrical power to run the additional electrical equipment as well as the standard aircraft subsystems.

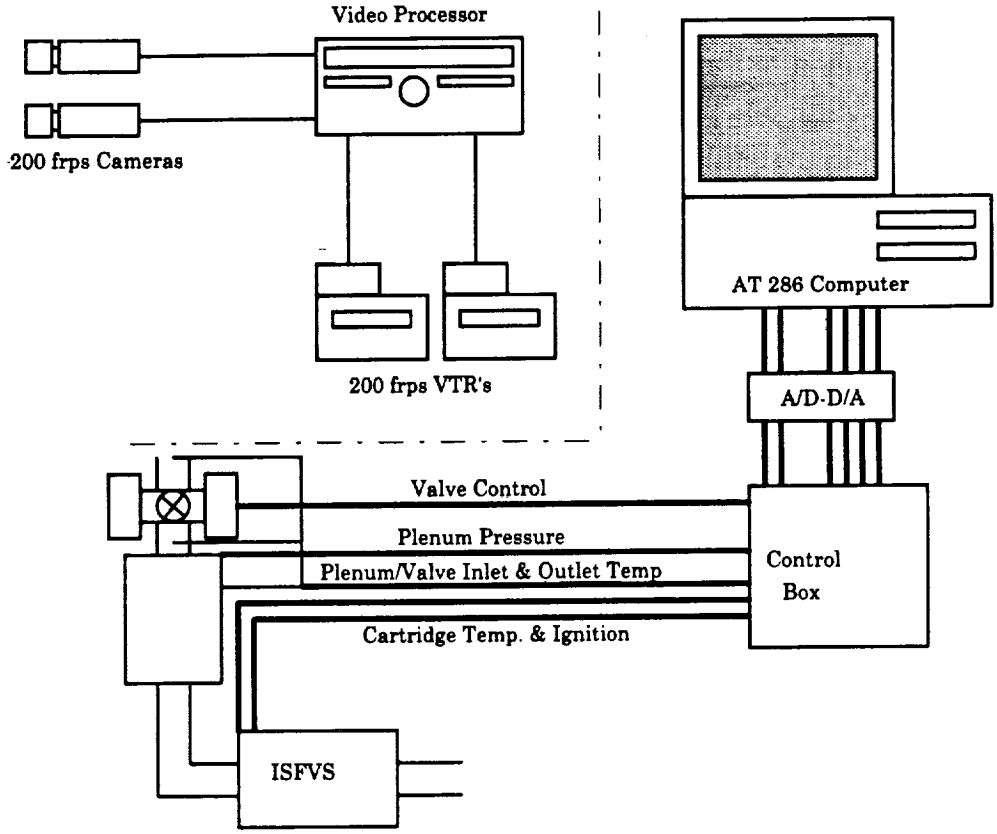

Figure 7: Schematic of Flight Test Data Collection Equipment

For this test, two 200 frps video cameras were used. Camera one was mounted on a tripod extending above the cabin of the aircraft. The camera was mounted so that it looked down upon the wing. Camera two was mounted on an existing camera mount attached to the left nacelle facing inboard. Both cameras used 7mm fixed aperture (f 2.0) wide angle lenses. Manually adjustable polarizing filters were used to control the aperture and reduce glare. A 52mm red #25 lens filter was installed on the top camera prior to Flight 8 in an attempt to increase contrast between the smoke and the background. Simple aluminum fairings were constructed around each camera to reduce drag and aerodynamic buffet. A third camera could have been mounted in the vertical tail, but due to the difficulty of installation, and the fact that this camera would have provided little more useful information because of its line-of-sight, it was omitted. Sufficient information to derive 3-D trajectories was available from the two cameras. All portions of the aircraft within the field of view of the cameras were painted flat black to provide a background contrast for the white smoke.

A small strake was mounted flush on the left side of the fuselage just forward of the wing leading edge. The strake, inclined at 15°, served to create a vortex into which the smoke was injected. The strake initially installed had a planform area of approximately 60 in^2, and was adjustable from the cockpit. The strake planform shape could be characterized as gothic, and was scaled to duplicate the first 6 ft of the F/A-18 LEX. A sweep angle was estimated by drawing a line between the

strake apex and the base. Using this approximation, the strake mounted on the Cougar had a leading edge sweep of approximately 75°. Prior to flight, concern was raised as to the effect of the strake on the Cougar's flying qualities. By providing a means of adjustment, the pilot could streamline the strake should flying qualities be objectionable, or severe structural vibration occur. Figure 8 illustrates the strake location on the left fuselage and the camera and tripod mountings.

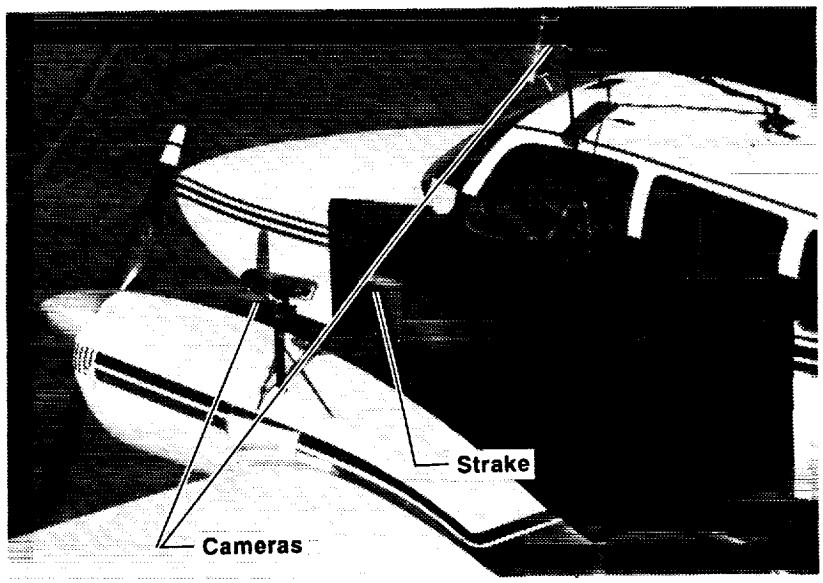

Figure 8: External Modifications Made to the GA-7

Table 2: Summary of Aircraft and Strake Geometry

Aircraft Geometry		Strake Geometry	
S_w	184 sq ft	S_s	120 in.^{2}
b_w	36.8 ft.	b_s	6.96 in.
c_{wr}	72 in.	c_{sr}	30 in.
c_{mac}	57 in.	i_s	15°
		Λ_{LE}	Gothic (~75°)

Table 2 summarizes the aircraft[5] and strake geometry. The small strake had no adverse effect on flying qualities. However, the vortex produced by the small strake was not well defined. The strake planform area was therefore doubled. Subsequent flights revealed that the large strake had no noticeable effect on flying qualities, although some airframe buffet was evident at the stall. This strake was fixed to the side of the fuselage at a 15° incidence angle. Vortical flow patterns produced by the large strake were found to be excellent, and it was the strake used for the remainder of the tests. All video data presented in this report were generated using the larger strake configuration.

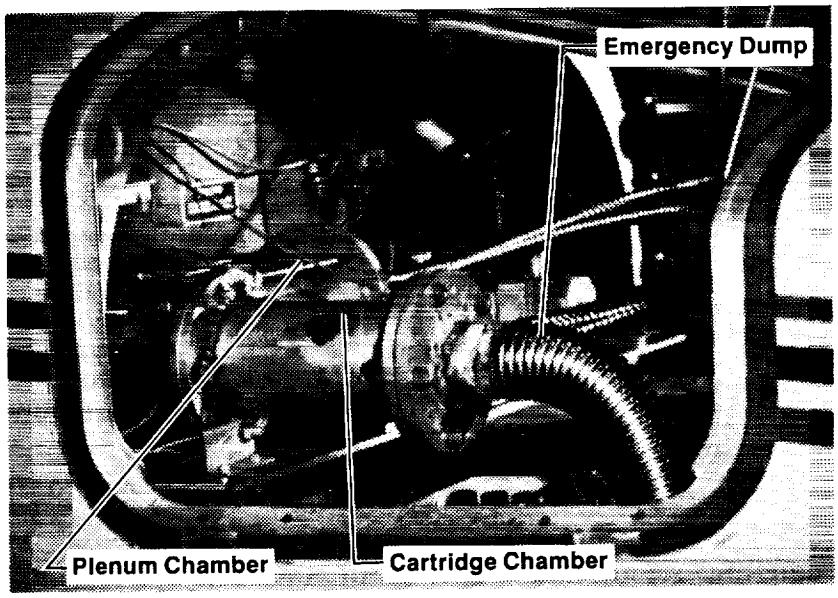

Figure 9: Right Side View of the Nose Baggage Compartment

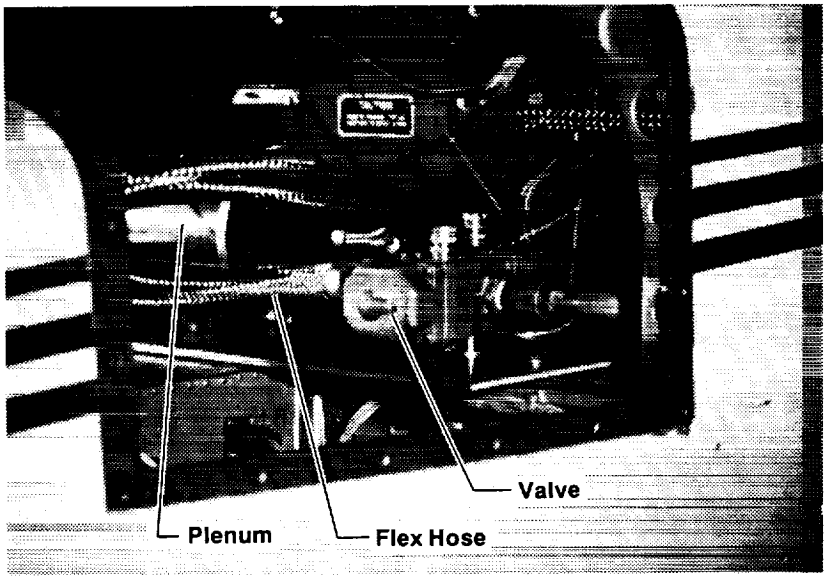

Figure 10: Left Side View of the Nose Baggage Compartment

The ISFVS was mounted in the nose baggage compartment to isolate it from the cockpit as well as allow ready access for removal and servicing. Figures 9 and 10 show the installation the ISFVS in the nose baggage compartment. Cooling vents were cut in the radome and fuselage bottom to remove heat from the compartment during ignition. The primary smoke exhaust port exited the side of the fuselage just forward of and below the apex of the strake, while the secondary port vented smoke out of the bottom of the aircraft - away from the area of prime interest. The over pressure exhaust duct was vented out the bottom right side of the aircraft. All external fresh air vents were closed off and sealed to reduce the likelihood of smoke entering the cockpit. The large plenum chamber (175.7 in^3) was used to allow the greatest margin of safety with respect to over-pressure conditions. (See the **Wind Tunnel Results,** pages 3-5.)

The valve control box was repackaged for the aircraft installation. The valve control and data collection software ATSMK was revised for use on the aircraft. The logic used to control the valve was unchanged from Myatt's original design[1].

The ISFVS was first installed in the GA-7 using a long flexible hose between the plenum chamber and the valve. After Repeated valve jams, this hose was thought to be causing significant cooling of the smoke mixture. The lower temperatures were producing excessive particulate matter, jamming the valve, according to this hypothesis. A much shorter, fixed tube assembly was used as a replacement. The shorter tube did not solve the problem, but it remained in the installation throughout the remainder of the tests.

Another modification to the original installation reduced the size of the primary (vortex seeding) orifice. The original design used a 1 inch o.d. outlet, while the modified design used a 9/16 inch o.d. opening. This change was made to concentrate the seeding of the vortex core.

Camera Calibration

After installation in the aircraft, the video imaging system was calibrated to determine camera positions and the regression coefficients used by the data reduction software. The calibration software required that a minimum of six non-coplanar control points be within the view of each camera. The location of each control point (X,Y,Z) was carefully determined from a user-defined origin (Figure 11).

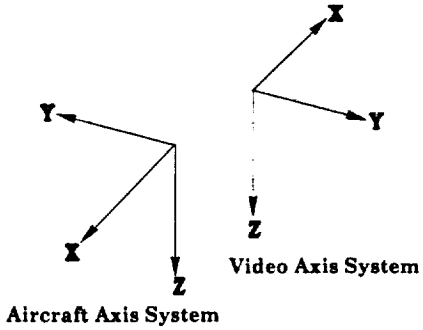

Figure 11: Comparison of Axis Systems

The axis system of the calibrated control volume was selected to align with the body axes of the aircraft. Note however that positive X points aft, positive Z is down, and positive Y is out the left wing. In other words the video system axes are parallel to, but rotated from the conventional aircraft axes system.

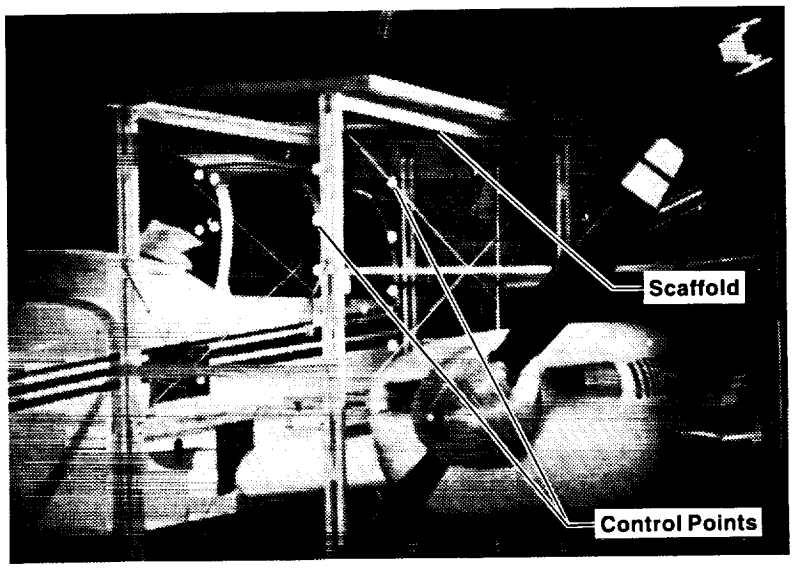

Figure 12: Camera Calibration Stand

A scaffold (Figure 12) was constructed over the top of the wing between the left side of the fuselage and the left nacelle. Four plumb lines were hung from pre-determined locations at the top of the scaffold. Each plumb line contained four spherical balls coated with reflective tape.

The aircraft was carefully leveled using an electronic protractor, and the control point locations were determined within ±0.03" using a 60" engineering scale. Ten frames of video were recorded from each camera, and digitized using the video data collection software.

Table 3: Summary of Camera Calibrations

		(all dimensions in inches)			
No.	Camera	X	Y	Z	Norm
1	1	45.80	2.34	-4.55	1.19
1	2	31.67	35.54	18.80	1.83
2	1	50.01	1.88	-11.58	1.01
2	2	33.65	40.41	17.83	1.10
3	1	49.83	2.65	-10.27	0.72
3	2	34.55	40.87	18.80	0.69

The camera calibration software module located the camera positions with respect to the chosen origin. Camera locations and residual norms for three separate calibrations are supplied in Table 3. Three calibrations were required

because the video imaging equipment was scheduled for use in another test. The equipment was removed from the aircraft on several occasions, and required recalibration upon subsequent installations. The first row of calibration data were used to reduce video data taken with the small strake configuration (Flights 1-5), while the second set of calibration data were used with the large strake video data (Flights 6-9). The third calibration set was used to reduce data from Flight 10.

The residual norms provide a measure of adequacy to each camera's calibration coefficients. The video software reference manual suggested that norms of approximately one or less were adequate. Except for the first calibration, Table 3 shows that all norms were within the tolerances specified. Significant errors in the measurement of the control point locations are thought to be the culprit leading to the poor residuals obtained during the first calibration.

Lens Aberration Errors

A potential source of error arising from the use of any camera based measurement system is that due to optical distortion. Several types of aberrations affect the image produced by a lens. Coma, astigmatism, field curvature, and spherical aberration affect the quality (i.e., clarity) of an image[6]. Distortion directly affects the off-axis, or transverse location of an image in the image plane. For this application, only distortion is of concern.

Lens distortion can be further categorized as symmetric radial, and asymmetric decentering distortion. Symmetric radial distortion is also known as barrel or pincushion distortion, and is readily apparent in ultra-wide angle, or "fish-eye" lenses. Asymmetric decentering distortion arises from the minute misalignment of the lens components within the lens body[6,7]. Analytical calibrations can be made to correct a specific camera/lens combination for both symmetric radial and asymmetric decentering distortion. An analytic method, taken from Brown[7], is described by Anderson[6].

Symmetric radial lens distortion is usually compensated using a polynomial curve fitting process[6]. Conrady's model is generally used to correct asymmetric decentering lens distortion[7]. Combining the analytic models for symmetric radial and asymmetric decentering distortion leads to the following equations for the correction of the focal plane coordinates

$$\Delta x = \bar{x}\left[l_1 r^2 + l_2 r^4 + l_3 r^6\right] + \left[p_1(r^2 + 2\bar{x}^2 + 2p_2\bar{x}\bar{y})\right]\left[1 + p_3 r^2\right] \tag{1}$$

$$\Delta y = \bar{y}\left[l_1 r^2 + l_2 r^4 + l_3 r^6\right] + \left[p_1(r^2 + 2\bar{y}^2 + 2p_2\bar{x}\bar{y})\right]\left[1 + p_3 r^2\right] \tag{2}$$

where

$\bar{x} = x - x_o$,

$\bar{y} = y - y_o$,

$r^2 = \bar{x}^2 + \bar{y}^2$,

l_1, l_2, l_3: symmetric radial distortion parameters,

p_1, p_2, p_3: radial and tangential asymmetric decentering parameters.

The distortion parameters, as well as x_o and y_o, can be estimated using a Least Squares Differential Correction (LSDC) routine as described in Anderson[6]. The derivation and description of the LSDC are included as Appendix A.

Lens distortion corrections were not made to data included in this paper. However, an analysis was done to determine how lens aberrations inherent in the 7mm lenses affected the trajectory and velocity measurements made with EV. Additionally, this analysis demonstrated the utility of the LSDC lens calibration procedure described in Appendix A.

Lens Calibration Demonstration

A single camera was aligned so that its line of sight (LOS) was orthogonal to a bare wall. A target grid was constructed by placing 1/4" diameter reflective tape "dots" at known polar locations within the field of view (FOV) of the camera. A total of 72 targets were included to fully populate the FOV of the camera. Twenty-five video frames of the target grid were digitized and averaged to compute mean centroid locations for each target. By assuming that distortion along the LOS of the lens was insignificant, video derived measurements of a target centered in the camera's FOV were used to determine a distance scaling factor. The scaling factor was used to convert the video's averaged centroid locations from pixels to inches so that direct comparisons could be made with the actual target coordinates. The scale factor calculated for this purpose was 0.1129 inches/pixel.

The LSDC routine described in Appendix A was utilized along with the known target locations and the converted video centroid data to generate the unknown distortion parameters. The routine typically converged within five iterations. Final values for the distortion parameters are listed below:

$$x_0 = -1.1879 \times 10^{-3} \text{ in}$$
$$y_0 = -1.8950 \times 10^{-3} \text{ in}$$
$$l_1 = -1.0031 \times 10^{-3} \text{ in}^{-2}$$
$$l_2 = 3.6232 \times 10^{-6} \text{ in}^{-4}$$
$$l_3 = 7.7828 \times 10^{-10} \text{ in}^{-6}$$
$$p_1 = -5.8425 \times 10^{-4} \text{ in}^{-1}$$
$$p_2 = 2.7086 \times 10^{-4} \text{ in}^{-1}$$
$$p_3 = -9.5932 \times 10^{-3} \text{ in}^{-2}$$

Using the estimated lens parameters, corrections were computed employing equations (1) and (2), and applied to the video derived centroid data. Figure 13 shows the actual target grid coordinates, the uncorrected video centroid data, and the centroids corrected for lens distortion.

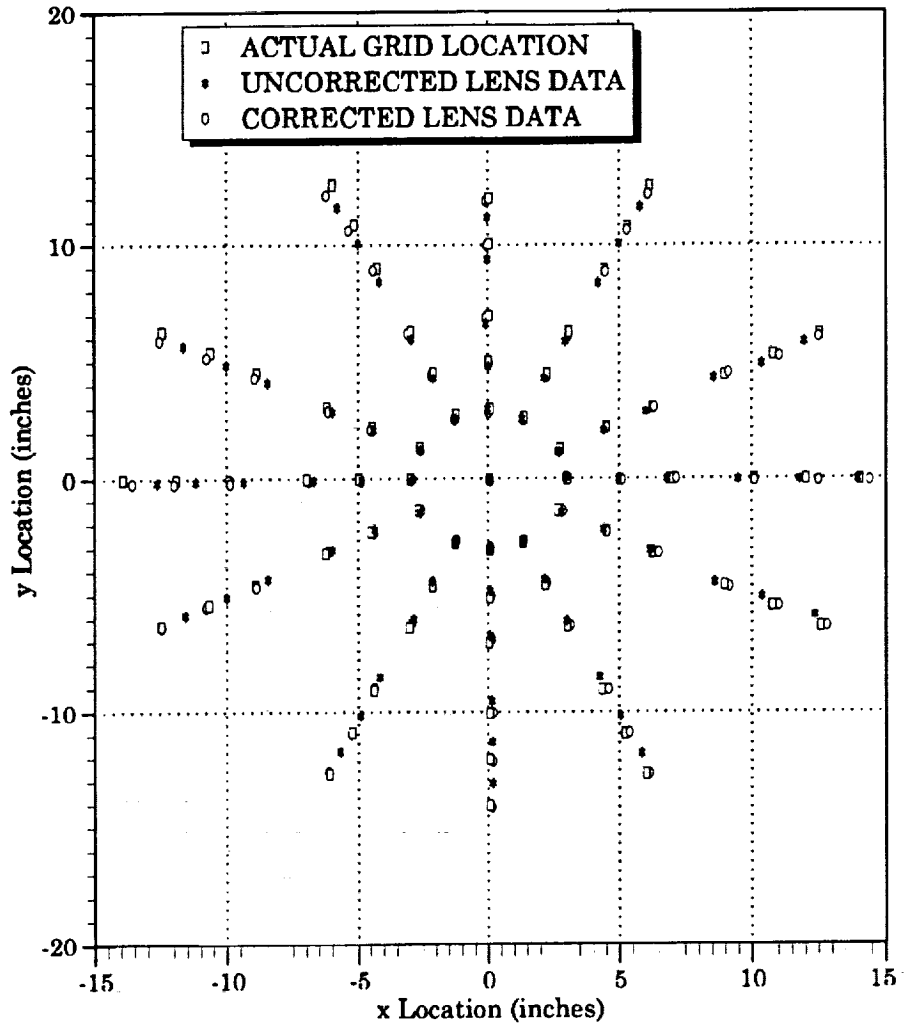

Figure 13: Illustration of Lens Aberration Effects and Corrections

Error Estimation

Errors induced by lens distortion were estimated using the data shown in Figure 13. Study of Figure 13 indicates that the left hand FOV of the 7mm lenses were more afflicted by distortion than the right hand side. From top to bottom, errors introduced by lens distortion were about equal. In each case, the distortion had the effect of "foreshortening" the actual location of the grid coordinate. This phenomenon is typical of barrel distortion.

The maximum error norm within the FOV of the lens before corrections were applied was 9.09%. After corrections, the maximum error norm was 5.56%. The actual errors at most locations within the FOV were much smaller. Overall, the error across the FOV was significantly reduced by applying the lens corrections.

Example of Lens Distortion Effects

Water tunnel data, collected during a separate test, were analyzed both with and without lens corrections. Notice that these data were only 2-D, collected using

a single camera mounting a 12.5mm lens. The distortion corrections for this lens are built into the video analysis software as a command option for use when computing centroids and paths. Therefore, the effects due to lens distortion on the trajectory and velocity data presented below are illustrative only. They are not representative of the errors induced in the 3-D flight data by the 7mm lenses.

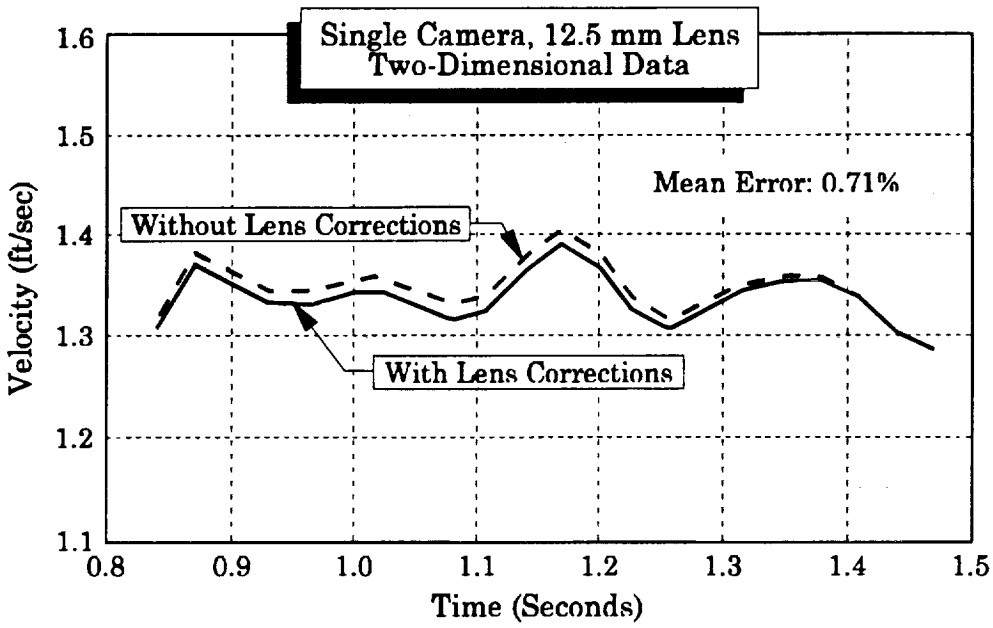

Figure 14: Lens Distortion Effects on Velocity Data

Figure 14 shows the velocity of a single pulse of dye as it traversed the test section at freestream velocity. A distance scale factor was computed for both the corrected and uncorrected cases. The "uncorrected" distance scale factor was 0.0601 inches/pixel, while the "corrected" distance scale factor was 0.0648 inches/pixel. The centroid, path, and velocity of the leading edge of the dye pulse were computed both with and without the built-in 12.5mm lens corrections. The appropriate distance scale factor was used for each case. The figure shows very little difference between the corrected and uncorrected velocity time histories. (The differences were less than 1%.) It was as though the lack of corrections in the calibration data canceled out the effects due to distortion in the actual vortex video data.

Errors were apparent in the trajectory data (Figure 15, page 16). The uncorrected trajectory data were elongated with respect to the corrected trajectory data - a consequence of pincushion distortion.

Test Procedure

The ISFVS valve dwell times and cycle times were digitally controlled. By sweeping the timing values over a small range, the leading edges of the smoke become visible to the cameras in a slightly different location during each puff. In this way, it was hoped that individual data points would "fill in" over a relatively

long period of time, and trends in the trajectory and velocity would become more discernible. This approach helped circumvent the liabilities imposed by using the relatively slow 200 frps cameras. Table 4 depicts the valve timing parameters that were used.

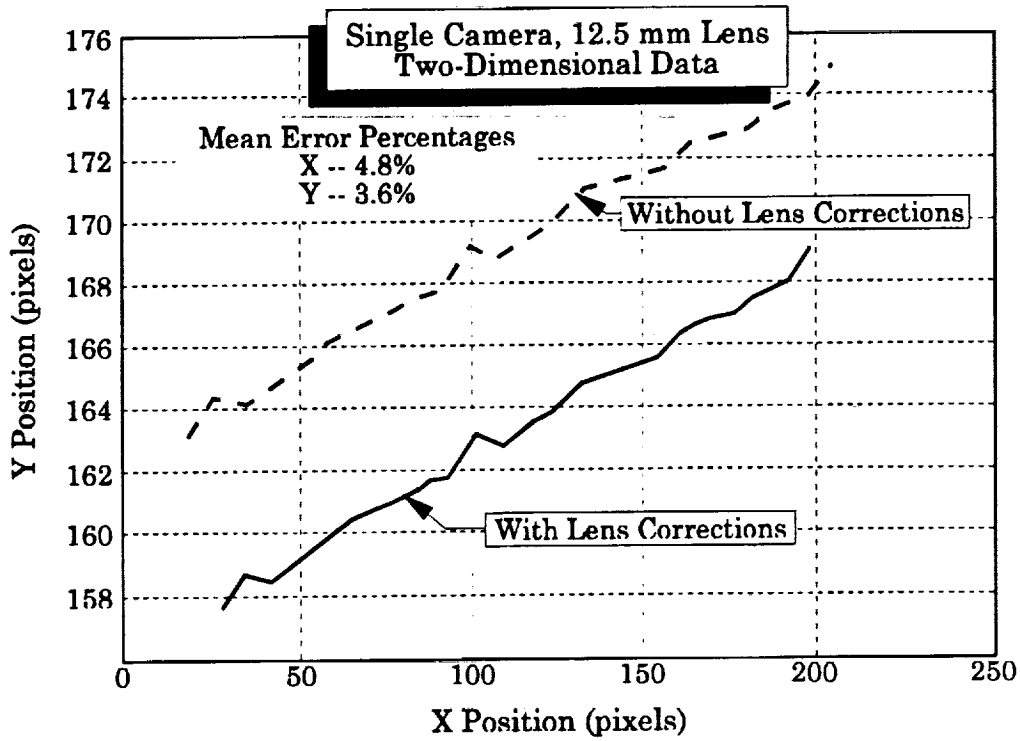

Figure 15: Lens Distortion Effects on Trajectory Data

Typically, ISFVS flight tests were carried out beginning at altitudes between 4000 and 6000 ft msl. The left engine was shut down, and its propeller feathered. The GA-7 would not maintain altitude on the remaining engine above 4000 ft, so the tests were accomplished during a slow descent.

Table 4: Summary of ISFVS Valve Timing Parameters

Sequence No.	Open Time (ms)	Dwell (ms)	No. Cycles
1	40	50	5
2	60	50	5
3	70	50	5

Note: Sequences repeat.

After completing the pre-ignition checklist, the aircraft was trimmed in level flight at approximately 75 - 80 KIAS. The pilot maintained a heading so the sun position did not degrade contrast levels. The smoke cartridge was fired, at which point the valve began cycling according to the pre-set cycle parameters. Typical cartridge burn time was between 30 seconds and one minute. The best quality

smoke was obtained approximately 20 seconds into each run, and lasted about 10 seconds. After the run, the left engine was restarted, and the aircraft returned for landing.

Aircraft weight during these tests was approximately 3800 lbs. The pitot-static system was not instrumented, but readings of cockpit instrumentation in flight combined with test day atmospheric conditions resulted in true airspeeds between 124 and 141 ft/sec. Using these conditions, along with wind tunnel data provided by Binford[8], trim AOA was 6.4°. Allowing for a small amount of upwash, as well as the strake incidence angle, local AOA at the strake was approximately 22.4° ± 1.6°. Typical Reynolds number values at flight condition were on the order of 2.0×10^6 based on strake chord.

A Piper PA-18 Super Cub was used as a chase aircraft during most flights to give video and still camera coverage external to the Cougar, providing qualitative data to determine whether the smoke adequately seeded the vortex core. The chase pilot also observed the early shakedown flights, looking for vibration or flutter.

Flight Test Results

The following sections present the results of the flight validation phase. The first section deals with the performance of the ISFVS system, while the second section presents analysis of the video data obtained during the flights.

ISFVS Performance

Each of the first nine flights experienced valve jams at some point during the cartridge burn. A valve jam was never recorded while carrying out ground tests.[8] Typically, the jam occurred during the period when smoke density was highest. At this point, the cartridge purged itself of ash, and plenum pressures and temperatures attained their maximum values. While usable video data were collected up to the time of the valve jam, the jam was unacceptable from a reliability standpoint. The HARV requires two cartridges to be burned simultaneously. Additionally, multiple firings are desired during any given flight. The goal is to have the system function nominally for at least six firings. The ISFVS valve was disassembled, cleaned, and lubricated prior to each firing for these nine developmental flights, when these valve jams occurred.

Figure 16 shows a characteristic time history of ISFVS plenum chamber differential pressure. Ground tests indicated maximum sustained plenum pressures to be 4.5 psid with the valve in the diversion mode[1]. This result is consistent with ISFVS flight data. The pressure spike is a peculiarity of the system resulting from the purging of ash during the smoke canister burn. Because the valve was operated in the diversion mode, no hazardous plenum pressures were recorded. During Flight 9, the rupture disk blew out due to a blockage in the tube between the cartridge chamber and the plenum. The blockage occurred due to inadequate cleaning of the system between flights.

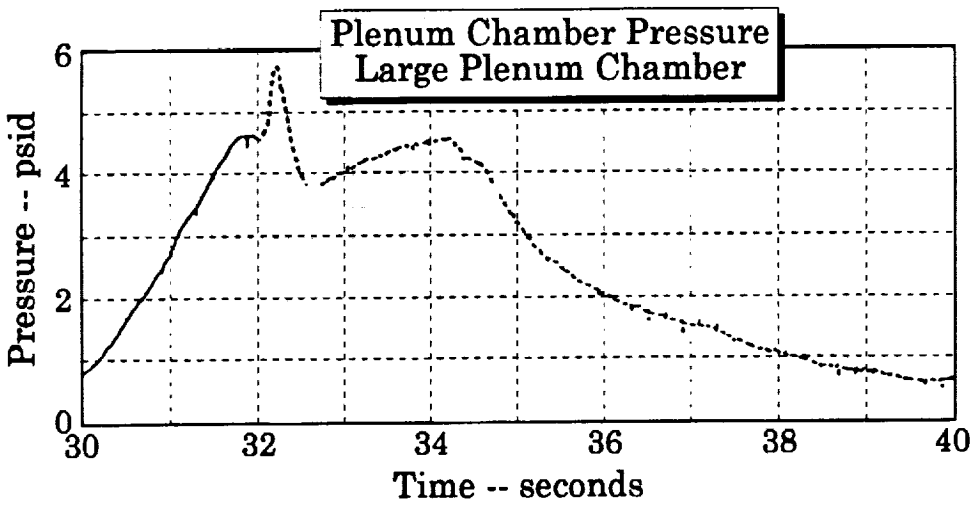

Figure 16: Typical Plenum Chamber Differential Pressure Variation

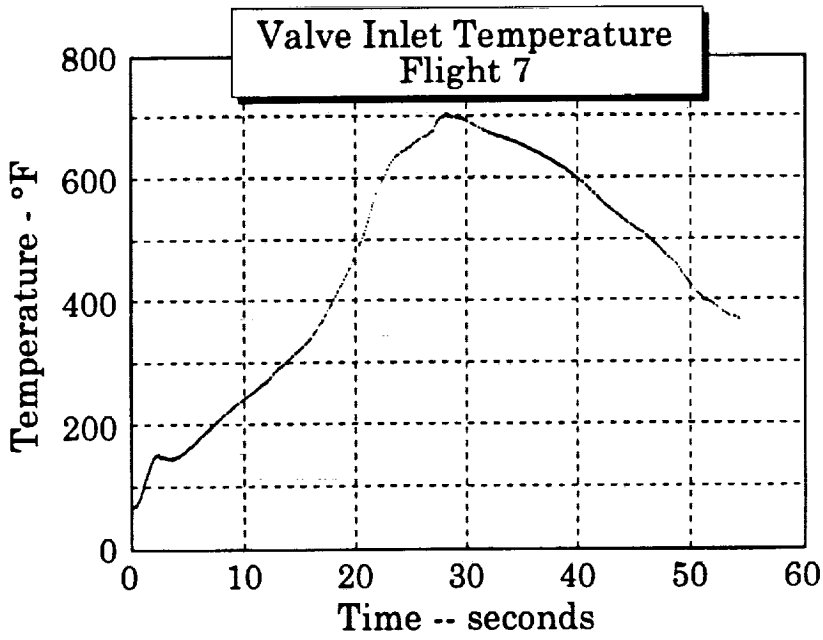

Figure 17: Typical Valve Inlet Temperature Variation

Figure 17 illustrates representative ISFVS valve inlet temperature behavior during ignition. Initially, peak temperatures were significantly lower than peak values obtained during ground tests[1]. It was thought that the valve jams were temperature related because peak valve inlet temperatures were below the published condensation temperature of terephthalic acid (572° F)[1]. Heaters were placed on the plenum and valve, and ceramic fiber cloth was used to insulate the ISFVS plumbing. Furthermore, the cooling air flow was reduced by covering one-half of the nose compartment air vent. The result was peak valve inlet temperatures in excess of 700° F. The valve still jammed.

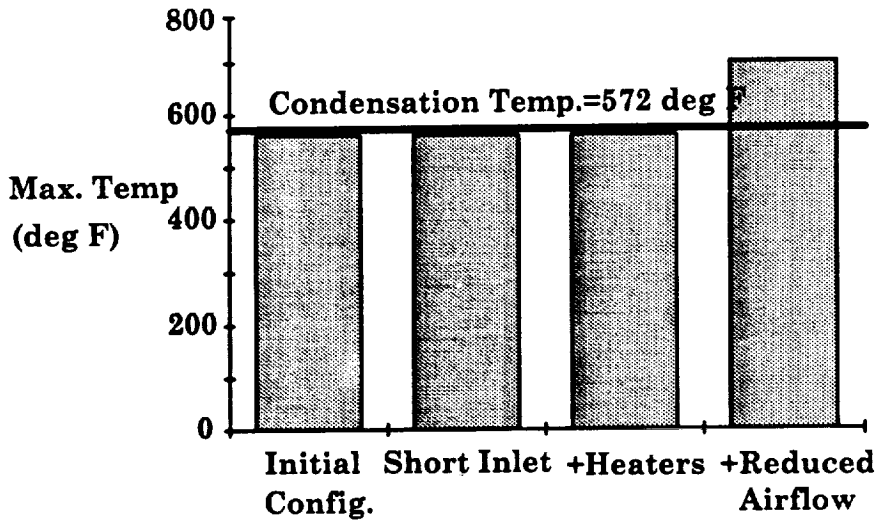

Figure 18: Maximum Temperatures for ISFVS Configurations Tested

Figure 18 shows peak valve inlet temperatures obtained for different ISFVS configurations. The reduced cooling air flow significantly increased peak temperatures, but the addition of the heaters had little effect on maximum temperatures. However, the heaters raised the initial temperatures by about 30 °F. Because the valve continued to jam after these modifications, temperature apparently was not the primary cause of the jams. Following these tests, the heaters and blankets were removed to allow easier maintenance of the system.

Valve lubrication was changed after Flight 8. Initially the valve had been lubricated using molybdenum based bearing grease. On later flights, the valve was lubricated with high temperature electric motor grease. A simple test, conducted by heating various lubricants on an aluminum plate and observing their reactions, revealed that high temperature, low viscosity aircraft bearing grease was by far the superior lubricant. A ground firing using this grease revealed no valve jams. Without cleaning the system, the ISFVS was fired again, and a jam occurred at the very end of the run. The high temperature grease was used as the valve lubricant for the remainder of the tests. A valve jam occurred on Flight 9 just prior to the rupture disk failure. However, because it was determined that inadequate cleaning of the system caused the failure, this was not considered a fair test of the lubricant. No valve jam occurred during Flight 10.

While use of high temperature bearing grease improved valve operation, it did not eliminate valve jams. Consequently, another smoke source that would produce little or no soot, while retaining the excellent visualization properties of terephthalic acid was sought.

A ground test of a US Army M-18 yellow smoke grenade showed that while it produced as large a volume of smoke as the NASA terephthalic acid grenade, very little residue was ejected. This test was not conducted using the ISFVS, but rather by simply burning a grenade in a can, and observing the remaining residue. Further research into the M-18 revealed that it contains carcinogenic materials, and may not be suitable[9].

Analysis of Video Data

Video data digitization and editing was painstakingly done using the video processor, the data collection software, and the video mask editor. Each frame of data was carefully edited to remove unwanted noise and background information. The leading edge of each individual smoke puff was identified such that the tracking software module could compute its centroid, and therefore the path of the vortex core.

Data presented here were taken over a very short period of time (2-3 seconds total) during specific runs. Therefore, it was assumed that the aircraft's flight condition remained constant during each data run. However, because true airspeed, AOA, and sideslip angle were not instrumented during these flights, variations in flight condition from flight to flight are not known precisely. The three flights from which video data are presented (Flights 7, 8 and 10) were flown under very similar conditions. It is likely that AOA and sideslip varied no more than a degree or two from flight to flight. This small variation undoubtedly is a source of scatter from one flight to another.

Myatt[2] and Bradley[10] discuss the effects of blowing momentum coefficient (C_μ) on LEX vortex behavior. Using mass flow and exit velocity data presented by Myatt[2], and assuming that the maximum sustained plenum chamber pressure was no greater than 4.5 psid, C_μ was calculated to be 4.7×10^{-5} during the Cougar flight tests. This value is three orders of magnitude less than the minimum C_μ found to effect strake vortex behavior[10].

Trajectory data were left in dimensional form due to the unconventional aircraft configuration. Traditional use of wing chord is not rational since the inclined strake was largely responsible for the vortex measured. Velocity data were non-dimensionalized by dividing by a freestream velocity value of 132.5 ft/sec.

Trajectories

Considerable uncertainty in the trajectory data are apparent from puff to puff. This uncertainty is partly due to the tedious task of editing the video data one frame at a time to identify the edges of smoke puffs within the vortex core. Editing was hampered by changing light conditions, and camera frame rates that were far too slow. Morris[3] and Nelson[4] both had similar difficulties in the laboratory.

Figure 19 (page 21) illustrates vortex core trajectory data obtained from Flight 10. Figures 20 (also on page 21) and 21 (page 22) are video frames taken from the top and side cameras respectively. Comparison of the trajectory data with the video frames (in a qualitative sense) indicates that digitization reproduced the 3-D trajectories faithfully. Note that direct comparisons cannot be made because the video frames represent camera lines of sight, not the coordinate system defined by the calibrations. The flow direction has been plotted to be representative of the video frames for ease of comparison.

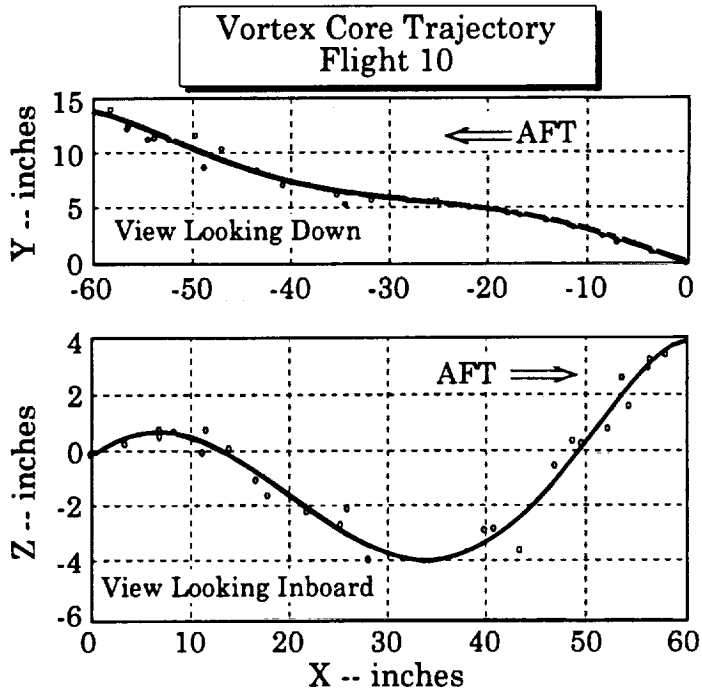

Figure 19: Vortex Core Trajectory

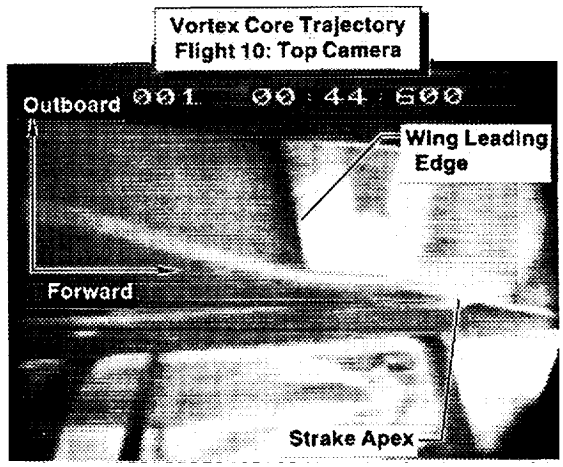

Figure 20: Vortex Core Viewed from the Top Camera

Data in Figure 19 were obtained by freezing an image of the vortex core on the video screen, and manually adjusting the video processor's threshold setting while taking single frames of digital data. This effectively "fooled" the video analysis software into "thinking" that movement was taking place, allowing the tracking algorithm to compute a path. Although no velocity data can be obtained using this technique, a more accurate core position can be determined because the user can control the contrast threshold to minimize changing lighting conditions.

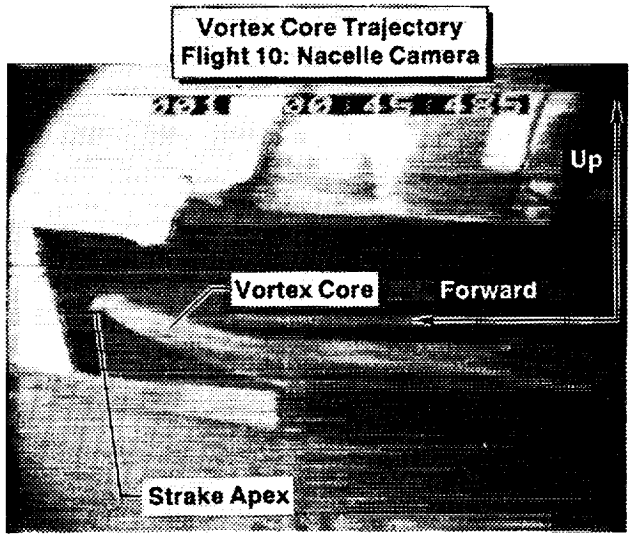

Figure 21: Vortex Core Viewed from the Nacelle Camera

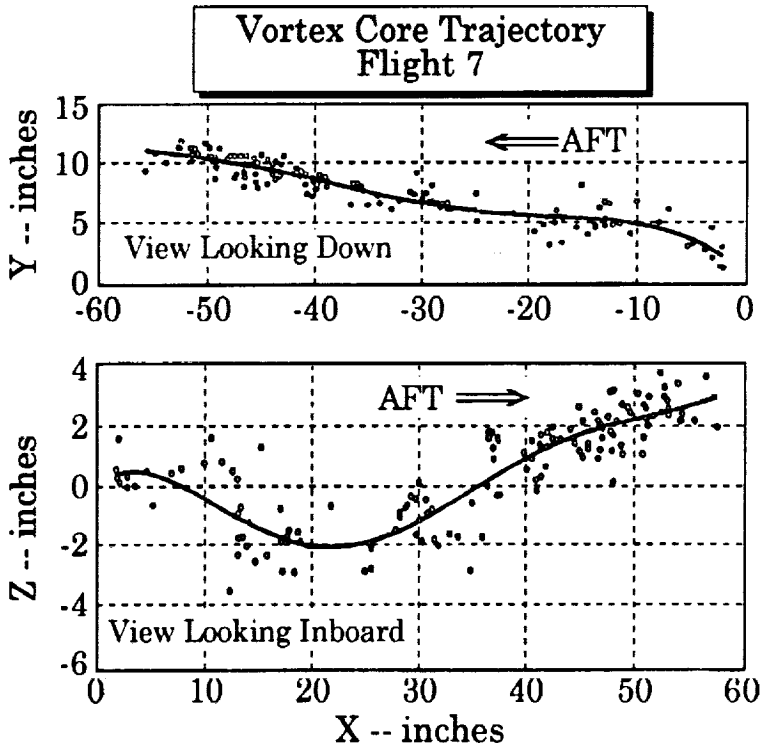

Figure 22: Typical Trajectory Data Used for Velocity Determination

Core Velocities

Figure 22 illustrates the time-matched trajectories (from Flight 7) that were used to derive the vortex core velocity profiles. Comparison of this figure with Figure 19 indicates that while the location of the vortex core in the X-Y plane was faithfully reproduced, the location in the vertical plane was not preserved as well. This discrepancy may be due to different flight conditions between Flights 7 and 10.

In any case, the general magnitudes and trends of Figure 19 are clearly repeated in this later trajectory.

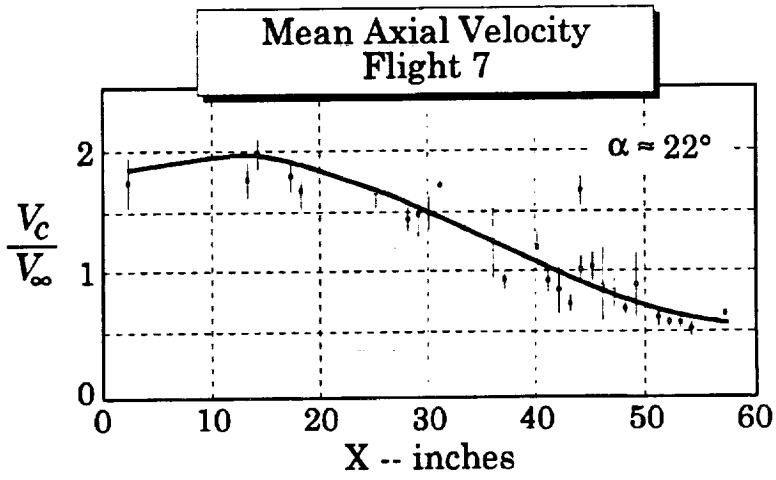

Figure 23: Typical Scatter in the Vortex Core Axial Velocity Profile

Figure 23 illustrates vortex core axial velocities obtained from Flight 7. Standard deviations in the core velocity profile were calculated by lumping all velocity data points within ±0.5 inches of a particular station, and then taking mean values of the collected points. Questionable points were removed from these data using Chauvenet's Criterion as described by Holman[11]. After the removal of wild points, the remaining X, Y and Z velocity data points were used to calculate a total velocity in the axial direction of the vortex core by taking the Euclidean norm. Standard deviations about the mean are shown as error bars on the plot. This figure illustrates the scatter in the velocity data, and is representative of data from Flights 8 and 10 also.

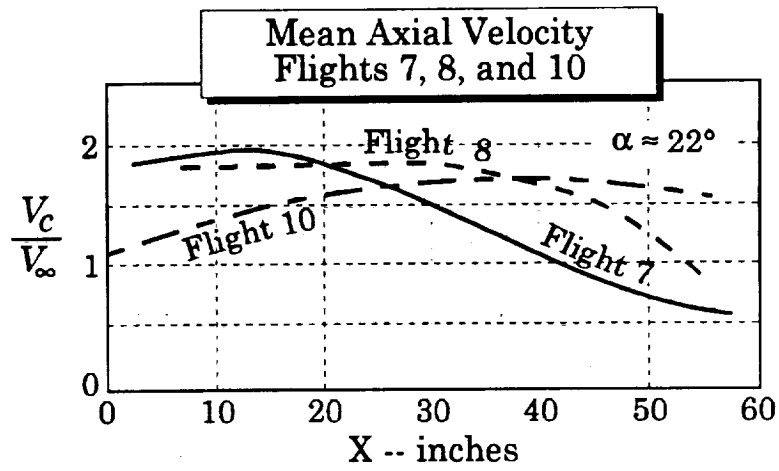

Figure 24: Axial Velocity Profiles from Three Flights

Figure 24 shows the best fit curves of axial core velocity taken from three different flights. Good repeatability was obtained between Flights 7 and 8, while Flight 10 indicated lower velocities upstream and higher velocities downstream.

These velocity ratios are consistent with those reported elsewhere (see Figure 25[3,13-18,20-22]). Although the strake/wing configuration tested here was considerably different than other delta wings tested, the insensitivity of vortex core axial velocity to configuration is apparent. This point was also made by Sforza[16].

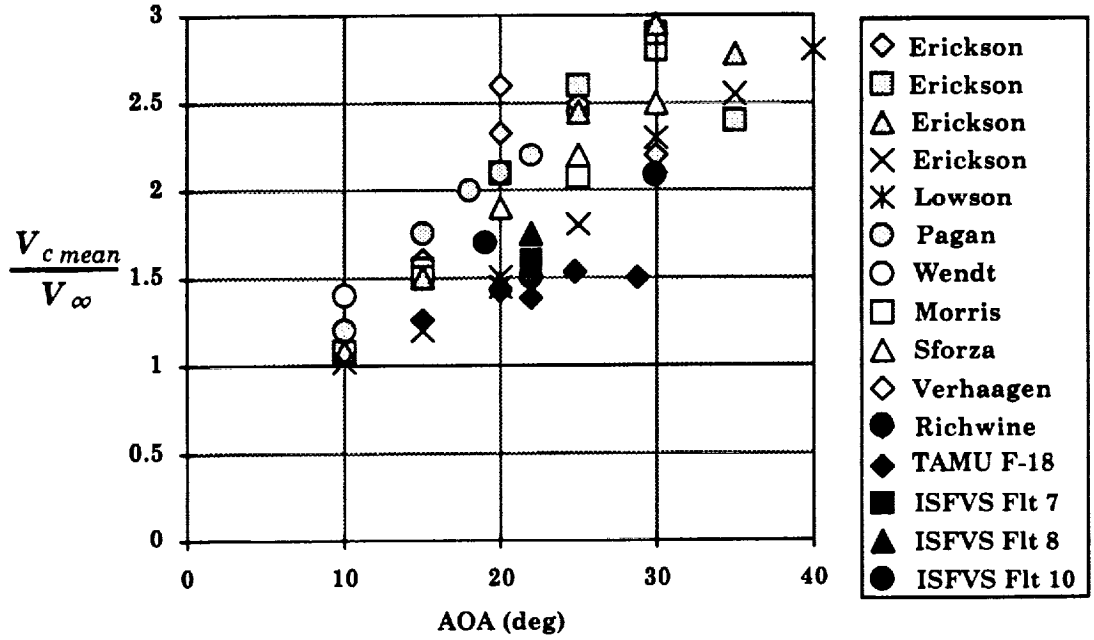

Figure 25: Comparison of Vortex Core Axial Velocities

Notice that the Richwine[21] data (● symbols in Figure 25) represent the axial velocities measured in the ring *around* the LEX vortex subcore, and not the stagnate subcore region. The LEX shape used for the ISFVS flight tests was similar to that of the F/A-18. The F-18 water tunnel data[22] (◆ symbols), the HARV rake survey data, and the ISFVS data all show good agreement. The lower core velocities obtained in the TAMU water tunnel are probably due to Reynolds number differences.

Pagan[12] and Lowson[13] reported that axial velocity in the vortex core remained constant up to the burst point. Lowson cited a constant axial core velocity ratio of 1.45 for a 70° delta wing at $\alpha = 20^\circ$ ($R_N = 6600$). Morris[3] and Pagan[12] both reported rapid decelerations in axial velocity near the burst point with negative axial velocities appearing after the vortex burst. Data presented by Vorropoulos[15] showed small velocity changes in the vortex core along the chord.

During the ISFVS tests, the strake vortex burst point lay just aft of the fields of view for both cameras. However, the very beginnings of vortex breakdown were evident by a gradual widening of the core around station 60. (The exact point where this widening began was difficult to define). These initial stages of vortex breakdown were particularly apparent during Flight 7, as substantiated by the deceleration of the axial core velocities shown in Figure 23. Variation of burst location from flight to flight may also reflect small AOA differences between flights.

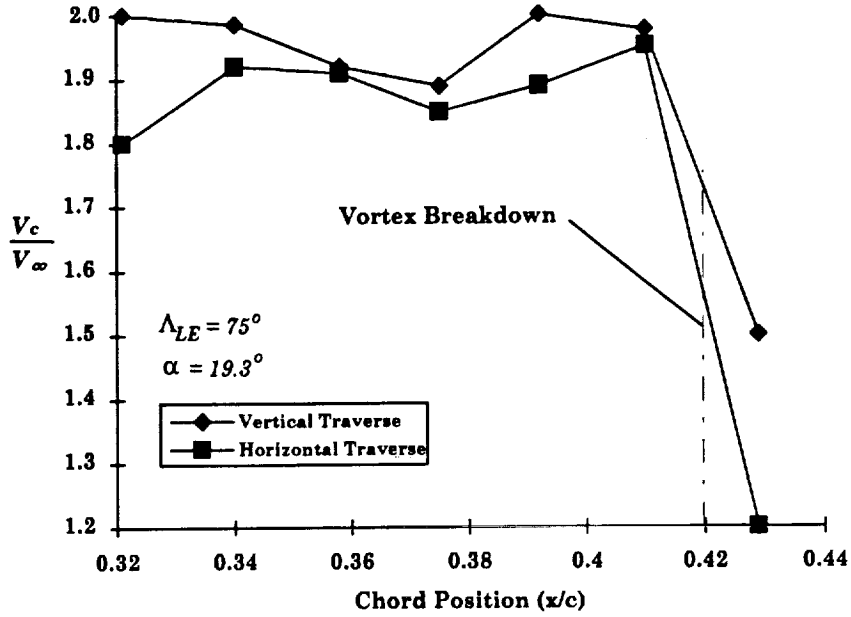

Figure 26: Axial Velocity Deceleration at Vortex Breakdown[13]

Figure 26 illustrates the typical axial deceleration apparent during vortex breakdown[12]. Similar results were observed in the water tunnel tests done in the TAMU water tunnel[22] (See Figures 20 and 21 in that document.) Figure 27 represents the mild variation of axial velocity along the chord prior to burst[14]. Even though the burst point was not visible in the fields of view for the cameras on the ISFVS test airplane, qualitative comparison of data from Flights 7 and 8 indicate core decelerations consistent with trends reported by other authors.

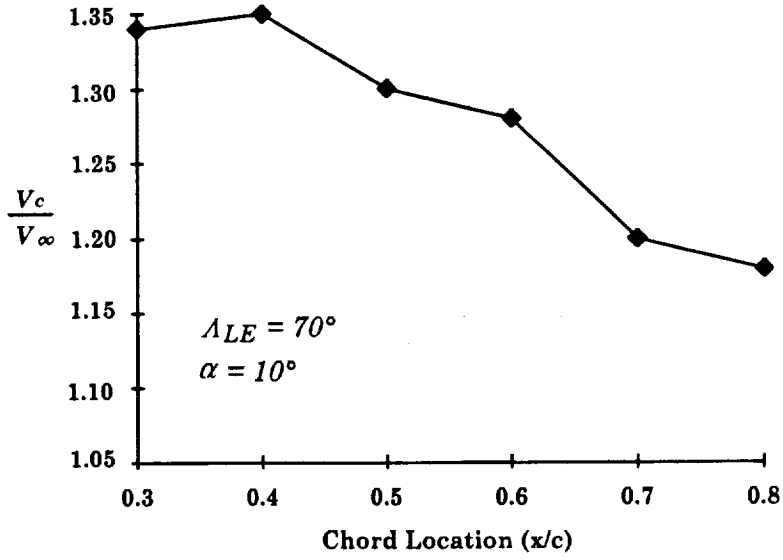

Figure 27: Velocity Ratio Variation with Chord[14]

Erickson[15] and others reported a variation of maximum vortex core axial velocity with Reynolds Number. Figure 28, adapted utilizing data from both Erickson[15] and Hall[18], depicts this variation. An ISFVS data point (from Flight 8), as well as data from the F/A-18 water tunnel test[22], have been added. Once again, the ISFVS data point agrees quite well with the other measurements. All the experimental velocity ratios are roughly 25% less theoretical predictions.

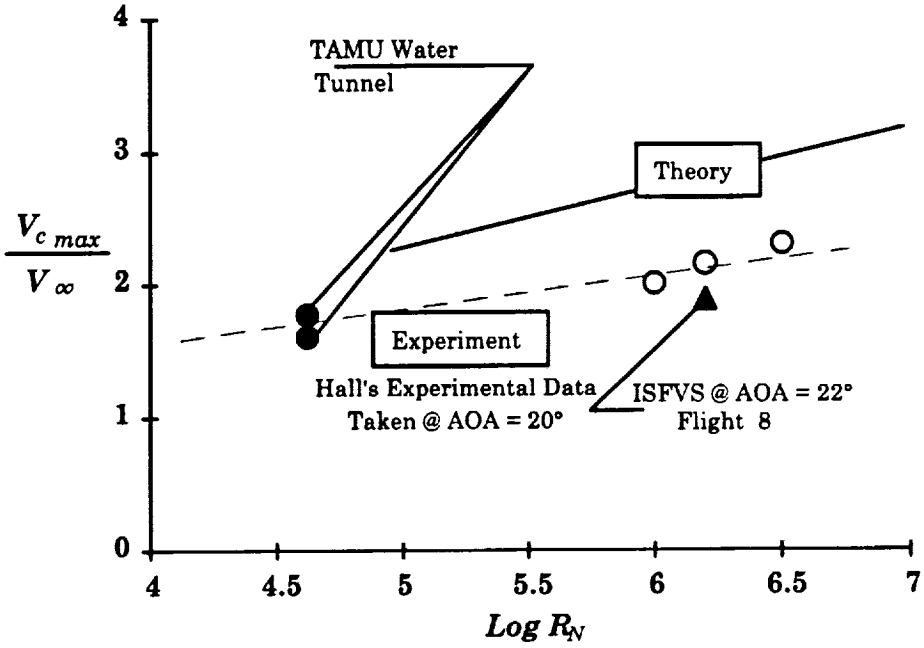

Figure 28: Axial Velocity Variation with Reynolds Number[15, 18]

Possible sources of error in the ISFVS data arise from lens aberration and inaccurate estimation of the Cougar's flight condition. Lens aberration primarily affects the trajectory data. Another possible source of error in the velocity data may be that the ISFVS smoke does not precisely seed the vortex subcore. Instead, centripetal forces most likely force the smoke out to some radial position from the core. This radial displacement is confirmed by the observation of a nearly hollow subcore on the video (Figures 20 and 21). Erickson[15] and Payne[20] also described this phenomenon. Data obtained by Pagan[12] for a 75° delta wing at 22° AOA indicated core velocity ratios on the order of 1.8 within 10 mm of the precise core of the vortex. This value is in good agreement with the ISFVS data. The peak core velocity ratio reported by Pagan[12] was 2.2.

Since the ISFVS velocity data likely represent the high energy ring of fluid surrounding the slender subcore of the vortex, the axially stagnate subcore reported by Richwine and Fisher[21] was not observed. The "hollow core" phenomena would explain the discrepancy.

EFFECT OF C_μ ON FOREBODY VORTICES

A survey of recent literature concerning control of forebody vortices by means of blowing indicates an extreme sensitivity of the lateral/directional moment coefficients to C_μ[23-26]. Peake's data[23] indicates a 300% change in the magnitude of C_Y (α = 16°) resulting from a C_μ of only 0.001 - referenced to cone base area. Guyton[25] presents data showing significant changes in C_n for values of C_μ as small as 0.003 (based on X-29 wing area[19]). Data collected and analysis done by Myatt[1] indicates that a typical operating value of C_μ for the ISFVS will be 3.8×10^{-5} (based on F/A-18 wing area). Table 5 summarizes minimum blowing momentum coefficients likely to have a significant effect on forebody vortex orientation. Due to differences between each configuration, the coefficients have been multiplied by their respective reference areas to allow direct comparisons.

Table 5: Summary of C_μ Forebody Data

Source	$C_\mu S$ (Min. Tested)	Notes
Peake[23]	0.0006	300% change in C_Y. Visible orientation changes.
Skow[24]	1.488	Sensitivity increased towards tip of nose.
Guyton[25]	0.555	Strong nozzle geometry effects.
Meyn[26]	0.340	$\alpha = 40^o$. Full scale F/A-18 water tunnel. test..
Myatt[1]	0.015	Maximum ISFVS C_μ.

Table 5 suggests that the ISFVS may have an effect on the forebody vortex orientation even though the value of C_μ is very small. Data presented by Peake[23] were obtained during a wind tunnel test of a cone at various AOA and values of C_μ. The ISFVS value of C_μ, based on F/A-18 forebody base area (taken at F.S. 180), is 0.0014 - greater than the value of 0.0012 shown by Peake to alter vortices over the cone. Except for Peake's data, the predicted ISFVS C_μ is an order of magnitude less than the minimum blowing momentum coefficients considered by the previous authors. Flow visualization photographs shown by Peake indicate a significant repositioning of the forebody vortex system for values of C_μ as small as 0.0012. Finally, the trend of increasing sensitivity as blowing is injected closer to the forebody apex is significant. Because the ISFVS ports must be located far forward on the HARV radome, any blowing effects will be further enhanced. Further study of this potential problem area is clearly warranted, considering the importance of understanding forebody vortex behavior. Careful measurements and further analysis are needed.

CONCLUSIONS AND RECOMMENDATIONS

Conclusions

The ISFVS, in conjunction with video imaging, was used to collect trajectory and axial core velocity data of a LEX vortex in flight. The LEX was operated at approximately 22^0 AOA and at a Reynolds number of 2×10^6 based on strake chord. The maximum axial velocity ratios were between 1.75 and 1.95 times freestream velocity. These values were in good agreement with velocity ratios obtained in water tunnels and wind tunnels for delta wings at 22^0 AOA. In particular, the ISFVS data exhibited good correlation with the F/A-18 water tunnel data, and the HARV rake survey data. The ISFVS velocity data followed trends with respect to Reynolds number apparent in other experimental data. Furthermore, the deceleration along the core axis near the vortex burst point showed good qualitative correlation with previously published data. The video derived trajectory data also exhibited good qualitative agreement with flow visualization photographs.

The maximum axial velocity ratios were slightly lower than some published data. This trend may be due to centripetal effects on the smoke particles within the vortex core, errors in the estimation of freestream flight conditions, or the unique configuration used in these tests.

The ISFVS can be used to determine the HARV LEX vortex trajectory and axial core velocity. Study of existing data indicates that the ISFVS mass injection rate may effect the forebody vortex orientation, which is especially sensitive to the momentum of the fluid injected into the boundary layer..

Recommendations

1. To improve ISFVS valve operation, an alternate smoke cartridge such as the M-18 or the 70-203 yellow smoke candle produced by E. Vernon Hill, Inc. of Benicia, CA should be substituted for the terephthalic acid grenade.

2. Higher speed video cameras (for example, 500 or 2000 frps) should be used to improve data quality. Alternatively, high speed motion picture cameras may be suitable for producing the needed high frame rates. Conversion of the motion picture data to video format may add uncertainty to the video images.

3. Heaters should be used in the ISFVS valve to improve operation at high altitude.

4. Lens calibrations should be applied to correct trajectory data for lens aberration errors. (See Appendix B for a detailed discussion of the procedure.)

5. Colored lens filters, as well as polarizing filters should be installed on the camera lenses to improve contrast between the smoke and its background. Filter color should be chosen to either darken the background (filter color contrasting with background) or lighten the smoke color (filter color same as smoke).

REFERENCES

[1]Ward, D. T., and Myatt, J. H., "Preliminary Design of an Intermittent Smoke Flow Visualization System," AIAA Paper 92-1028, Feb. 1992.

[2]Myatt, J. H., "Ground Validation of an Intermittent Flow Visualization System," Masters Thesis, TAMU Aerospace Engineering, Aug. 1991.

[3]Morris, Stephen L., "A Video Based Experimental Investigation of Wing Rock," Ph.D. Dissertation, TAMU Aerospace Engineering, Aug. 1989.

[4]Nelson, Michael D., "An Experimental Investigation of Leading Edge Vortical Flow About a Delta Wing During Wing Rock," Masters Thesis, TAMU Aerospace Engineering, Dec. 1991.

[5]Taylor, John, ed., *Jane's All the World's Aircraft 1977-1978*, Jane's Yearbooks, London, 1977.

[6]Anderson, David S., "Autonomous Star Sensing and Pattern Recognition for Spacecraft Attitude Determination", PhD. Dissertation, TAMU Aerospace Engineering, May 1991, pp. 61-66, pp. 118-135.

[7]Brown, D. C., Decentering Distortion of Lenses", Annual Convention of the American Society of Photogrammetry, Vol. 41, Washington, D. C., 1965, pp. 444-462.

[8]Binford, R. S., and Ward, D. T., "A Wind Tunnel Investigation of the Effects of Flow Energizers on the Performance of a Typical General Aviation Light Twin Aircraft," TEES Report No. TR-8334, vol. 1, TAMU Aerospace Engineering, March 1984.

[9]Private Communications with J. Domanico, CRDEC, Aberdeen, MD, May 1992.

[10]Bradley, R. G., and Wray, W. O., "A Conceptual Study of Leading-Edge-Vortex Enhancement by Blowing," *Journal of Aircraft*, Vol. 11, No. 1, Jan. 1974, pp. 33-38.

[11]Holman, J. P., *Experimental Methods for Engineers*, McGraw-Hill, New York, 1984, p. 73..

[12]Pagan, D., and Benay, R., "Vortex Breakdown Induced by an Adverse Pressure Gradient - Experimental and Numerical Approaches," AIAA Paper 87-2487, 1987.

[13]Lowson, M. V., "Visualization Measurements of Vortex Flows," AIAA Paper 89-0191, Jan. 1990.

[14]Vorropoulos, G., and Wendt, J. F., "Laser Velocimetry Study of Compressibility Effects on the Flow Field of a Delta Wing," AGARD-CP-342, Paper No. 9., 1983.

[15]Erickson, G. E., "Vortex Flow Correlation," AFWAL-TR-80-3143, 1980.

[16]Sforza, P. M., et al, "Flow Measurements in Leading-Edge Vortices," *AIAA Journal*, Vol. 16, No. 3, March 1978, pp. 218-224.

[17]Verhaagen, N. G., and Ransbeeck, P., "Experimental and Numerical Investigation of the Flow in the Core of a Leading Edge Vortex," AIAA Paper 90-0384, 1990.

[18]Hall, M. C., "A Theory for the Core of a Leading Edge Vortex," *Journal of Fluid Mechanics*, Vol. 11, 1961, pp. 209-228.

[19]Webster, D., and Purifoi, D., "X-29 High-α Flying Qualities," AFFTC-TR-91-15, July 1991.

[20]Payne, F. M., et al, "Visualization and Flow Surveys of the Leading Edge Vortex Structure on Delta Wing Planforms," AIAA Paper 86-0330, 1986.

[21]Richwine, D., and Fisher, D., "In-Flight Leading-Edge Extension Vortex Flow-Field Survey Measurements on a F-18 Aircraft at High Angle of Attack," AIAA Paper 91-3248, Sept. 1991.

[22]Dorsett, K. M., "Validation of an In-Flight Flow Visualization Scheme to Quantitatively Measure Vortical Flow Phenomena", TAMU Masters Thesis, Dec. 1992.

[23]Peake, David J., et al, "Control of Forebody Vortex Orientation to Alleviate Side Forces," AIAA Paper 80-0183, Jan. 1980.

[24]Skow, A.M., et al, "Control of Forebody Vortex Orientation to Enhance Departure Recovery of Fighter Aircraft," *Journal of Aircraft*, Vol. 19, No. 10, Nov. 1982, pp. 812-819.

[25]Guyton, B., et al, "X-29 Forebody Blowing Wind Tunnel Results," NASA CP 3137, Vol. 3, April 1992, pp. 283-344.

[26]Meyn, L. A., et al, "Full-Scale Wind Tunnel Tests of an F/A-18," NASA-CP-3137, Vol. 3, April 1992, pp. 199-222.

[27]Junkins, J. L., *An Introduction to Optimal Estimation of Dynamical Systems*, Sijthoff & Noordhoff International Publishers B. V., Alphen Aan Den Rijn, The Netherlands, 1978.

[28]"ExpertVision User's Manual," Motion Analysis Corporation, Santa Rosa, California, 1989.

APPENDIX A: LENS CALIBRATION PROCEDURE USING LSDC

The following Least Squares Differential Correction (LSDC) derivation and lens calibration procedure are taken from Anderson[6] and Junkins[27]. The familiar least squares estimation algorithm is derived as a starting point for the LSDC derivation. In this appendix vectors are lower case bold symbols and matrices are upper case bold symbols. Scalars are in normal fonts. The matrix transpose operation is denoted by ^{T}.

Least Squares Estimation

Consider a linear model

$$\acute{\mathbf{y}} = \mathbf{A}\mathbf{x} + \mathbf{e} \tag{A1}$$

where $\acute{\mathbf{y}}$ = (mx1) vector to be measured,

$\mathbf{A}$ = (mxn) known constant matrix,

$\mathbf{x}$ = (nx1) vector of unknown parameters,

$\mathbf{e}$ = vector of residual errors.

The method of least squares seeks an optimum choice of parameters $\mathbf{x}$ that minimizes the sum square of the residuals

$$\phi = \mathbf{e}^T\mathbf{e}. \tag{A2}$$

From (A1), $\mathbf{e} = \acute{\mathbf{y}} - \mathbf{A}\mathbf{x}$. Equation (A2) can then be rewritten

$$\phi = \acute{\mathbf{y}}^T\acute{\mathbf{y}} - \acute{\mathbf{y}}^T\mathbf{A}\mathbf{x} - \mathbf{x}^T\mathbf{A}^T\acute{\mathbf{y}} + \mathbf{x}^T\mathbf{A}^T\mathbf{A}\mathbf{x}. \tag{A3}$$

Note that each term in (A3) is a scalar. Since a scalar is its own transpose, the quadratic form of ϕ is written

$$\phi = \acute{\mathbf{y}}^T\acute{\mathbf{y}} - 2\acute{\mathbf{y}}^T\mathbf{A}\mathbf{x} + \mathbf{x}^T\mathbf{A}^T\mathbf{A}\mathbf{x}. \tag{A4}$$

We wish to find $\mathbf{x}$ which minimizes ϕ. A necessary condition to minimize ϕ is

$$\nabla_x\phi = -2\mathbf{A}^T\acute{\mathbf{y}} + 2\mathbf{A}^T\mathbf{A}\mathbf{x} = 0. \tag{A5}$$

The sufficient condition for Equation (A5) to be a minimum is

$$\nabla^2_x\phi = 2\mathbf{A}^T\mathbf{A} \tag{A6}$$

must be positive definite.

From (A5)

$$\mathbf{x} = (\mathbf{A}^T\mathbf{A})^{-1}\mathbf{A}^T\acute{\mathbf{y}}. \tag{A7}$$

Equation (A7) serves as the common basis for algorithms for solution of least squares problems. A more general form of (A7) includes a symmetric, positive definite weighting matrix **W**. The problem then becomes the minimization of

$$\phi = \mathbf{e}^T\mathbf{W}\mathbf{e}. \tag{A8}$$

W is usually taken to be the inverse of the measurement covariance matrix Λ_{yy}. Following reasoning analogous to the above derivation, the value of **x** that minimizes ϕ is

$$\mathbf{x} = (\mathbf{A}^T\mathbf{W}\mathbf{A})^{-1}\mathbf{A}^T\mathbf{W}\acute{\mathbf{y}}. \tag{A9}$$

Notice that (A7) is really just a special case of (A9) with $\mathbf{W} = \mathbf{I}$. We will refer to Equation (A9), and to the reasoning behind its derivation, frequently.

Least Square Differential Correction for Nonlinear Problems

Consider *m* observable quantities modeled as

$$y_j = F_j(x_1, x_2, ..., x_n);\ j = 1, 2, ..., m;\ m \geq n \tag{A10}$$

where $F_j(x_1, x_2, ..., x_n)$ are *m* arbitrary independent functions of the unknown parameters x_i. We wish to find a particular vector of x-values

$$\mathbf{x}^T = \{x_1, x_2, ..., x_n\} \tag{A11}$$

that minimizes the weighted sum square of the residuals

$$\phi = \Delta\mathbf{y}^T\mathbf{W}\Delta\mathbf{y} \tag{A12}$$

where

$$\Delta y_j = \acute{y}_j - F_j(x_1, x_2, ..., x_n);\ j = 1, 2, ..., m, \tag{A13}$$

W = (*m*x*m*) observation weighting matrix (Λ_{yy}).

For most practical problems, ϕ cannot be directly minimized by application of ordinary calculus to (A12). For that reason, a successive approximation procedure is used to converge to accurate least square estimates, given approximate starting values. At any point in the iteration, current estimates can be written as:

$$\mathbf{x}_c^T = \{x_{1c}, x_{2c}, ..., x_{nc}\}. \tag{A14}$$

The actual least square estimates $\{x_i\}$ are related to the current values by an unknown set of corrections $\{\Delta x_i\}$

$$x_i = x_{ic} + \Delta x_i;\ i = 1, 2, ..., n. \tag{A15}$$

Assuming that the Δx_i are small, it is possible to solve for their approximate values. The residuals corresponding to the current x-estimates are

$$\Delta y_{jc} = \hat{y}_j - F_j(x_{1c}, x_{2c}, ..., x_{nc}); j = 1, 2, ..., m. \quad \text{(A16)}$$

For small corrections Δx_i, the linearly predicted residual vector Δy_p (after the correction) comes from Taylor series expansions of (A13) about x_c

$$\Delta y_p = \Delta y_c - \mathbf{A}\Delta\mathbf{x} \quad \text{(A17)}$$

where $\Delta y_c^T = \{\Delta y_{1c}, \Delta y_{2c}, ..., \Delta y_{mc}\}$ = current residuals,

$\Delta y_p^T = \{\Delta y_{1p}, \Delta y_{2p}, ..., \Delta y_{mp}\}$ = linearly predicted residuals, after correction,

$\mathbf{A} = [\partial F_j/\partial x_i|_c]$ = (mxn) matrix of partial derivatives, evaluated with the current x-estimates, x_c. (A18)

Recall that we wish to determine the approximate corrections Δx_i such that the sum square of the linearly predicted residuals is minimized

$$\phi_p = \Delta y_p^T \mathbf{W} \Delta y_p. \quad \text{(A19)}$$

If this process is convergent, we would expect Δx to decrease on successive iterations until the linearization is an accurate approximation. Substitution of (A17) into (A19) yields

$$\phi_p = \Delta y_p^T \mathbf{W} \Delta y_p = (\Delta y_c - \mathbf{A}\Delta\mathbf{x})^T \mathbf{W} (\Delta y_c - \mathbf{A}\Delta\mathbf{x}). \quad \text{(A20)}$$

Minimization of this quadratic form is analogous to the minimization of (A4). Application of the necessary and sufficient conditions for minimization yields

$$\Delta\mathbf{x} = (\mathbf{A}^T\mathbf{W}\mathbf{A})^{-1}\mathbf{A}^T\mathbf{W}\Delta y_c \quad \text{(A21)}$$

where $\Delta\mathbf{x}$ = vector of parameter updates,

Δy_c = current residuals.

Use of the LSDC to Determine Lens Distortion Parameters

Equations (1) and (2) from the text are repeated below

$$\Delta x = \bar{x}\left[l_1 r^2 + l_2 r^4 + l_3 r^6\right] + \left[p_1(r^2 + 2\bar{x}^2 + 2p_2\bar{x}\bar{y}\right]\left[1 + p_3 r^2\right] \quad \text{(A22)}$$

$$\Delta y = \bar{y}\left[l_1 r^2 + l_2 r^4 + l_3 r^6\right] + \left[p_1(r^2 + 2\bar{y}^2 + 2p_2\bar{x}\bar{y}\right]\left[1 + p_3 r^2\right] \quad \text{(A23)}$$

where $\bar{x} = x - x_o$,

$\bar{y} = y - y_o$,

$r^2 = \bar{x}^2 + \bar{y}^2$,

l_1, l_2, l_3: symmetric radial distortion parameters,

p_1, p_2, p_3: radial and tangential asymmetric decentering

The parameter vector **x** is now replaced by **p** defined below

$$\mathbf{p}^T = \{x_o\ y_o\ l_1\ l_2\ l_3\ p_1\ p_2\ p_3\}. \tag{A24}$$

The reader should not confuse the scalar lens coordinates (x,y) with the vectors **x** and **y**.

Computation of **A**

Explicit expressions for the partial derivatives making up **A** can be derived. However, due to the occurrence of the x_o and y_o terms throughout the equations, this would be extremely tedious. Instead, a numerical approach that utilizes a difference method can be applied.

Perturb the ith value of **p** by a small value ε, holding all other parameters constant. Calculate **y** with the perturbed vector **p**; then the ith *column* of **A** is:

$$A(j,i) = (y_{new} - y_o)/\varepsilon;\ j = 1, 2, ..., m \tag{A25}$$

where y_{new} = perturbed value of **y**,
y_o = unperturbed value of **y**,
ε = amount ith column of **p** is perturbed.

This process is repeated until all eight parameters have been individually perturbed, and the **A** matrix is fully populated.

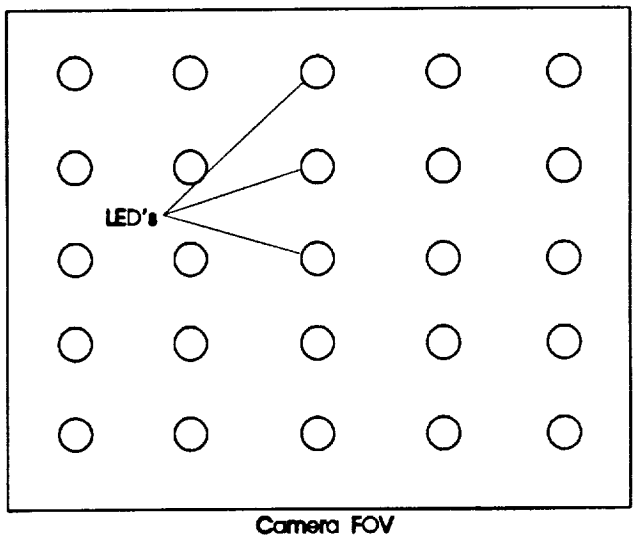

Figure 29: Lens Calibration Grid

The calibration procedure then proceeds as follows:

1. Figure 29 illustrates a suggested lens calibration grid. Obtain multiple video frames of a 2-D calibration grid containing *n* targets with known (x, y) coordinates. Average the resulting video files together to minimize the effect of "pixel twinkle" that is inherent with EV. This procedure can be carried out using the EV operator MERG[28]. Use the resulting *averaged* video file as the calibration file.

The center target in the grid must be carefully aligned with the camera LOS. The camera LOS should be as nearly perpendicular to the target plane as possible. Determine the centroid of each calibration target using the EV operator CENT[28]. The (x,y) coordinates now represent the target centroid coordinates.

Form the measurement vector

$$\acute{\mathbf{y}}^T = \{\Delta x(1)\ \Delta y(1)\ \Delta x(2)\ \Delta y(2)\ \ldots\ \Delta x(n)\ \Delta y(n)\},\ n = \#\ \text{targets} \tag{A26}$$

where $\Delta x_i = x_{i\ \text{video}} - x_{i\ \text{actual}};\ i = 1, 2, \ldots, n,$

$\Delta y_i = y_{i\ \text{video}} - y_{i\ \text{actual}};\ i = 1, 2, \ldots, n.$

2. Obtain the weighting matrix $\mathbf{W} = \{W_{ij}\}$

$$\mathbf{W} = \Lambda_{yy}^{-1}. \tag{A27}$$

3. Input parameter starting estimates

$$\mathbf{p}_c^T = \{x_o\ y_o\ l_1\ l_2\ l_3\ p_1\ p_2\ p_3\}. \tag{A28}$$

4. Compute current values of $\mathbf{y}_c$

$$\mathbf{y}_c = F(\mathbf{p}_c) \Rightarrow F \text{ is defined in equations (A22) and (A23).} \tag{A29}$$

5. Compute $\mathbf{A}$ (m x n) using the difference method previously discussed

$$\mathbf{A} = \frac{\partial F_j}{\partial p_i} \text{ evaluated at } \mathbf{p}^c. \tag{A30}$$

6. Form the residual vector

$$\Delta \mathbf{y}_c = \acute{\mathbf{y}} - \mathbf{y}_c, \tag{A31}$$

and their weighted sum-square

$$\phi_c = \Delta \mathbf{y}_c^T \mathbf{W} \Delta \mathbf{y}_c. \tag{A32}$$

Go to step (9) upon convergence. Convergence is evidenced by negligible changes in ϕ_c.

7. Determine the correction vector $\Delta\mathbf{p}$ which minimizes the predicted residuals sum squares

$$\Delta \mathbf{p} = (\mathbf{A}^T \mathbf{W} \mathbf{A})^{-1} \mathbf{A}^T \mathbf{W} \Delta \mathbf{y}_c. \tag{A33}$$

8. Apply the corrections to the original parameter estimates

$$\mathbf{p}_{c\ \text{updated}} = \mathbf{p} + \Delta \mathbf{p}. \tag{A34}$$

Go to step (4).

9. Set $\mathbf{p}_{final} = \mathbf{p}_c$ for the final iteration.

The final parameter values can now be used to model lens distortion. Each frame of video data can be corrected using equations (A22) and (A23) and the parameter estimates obtained above

$$x_{corr} = x + \Delta x, \tag{A35}$$

$$y_{corr} = y + \Delta y. \tag{A36}$$

This procedure can be easily automated using a FORTRAN program along with the EV file handling subroutines BOPEN and BCLOSE[28]. Each video file (denoted by *filename*.VID) should be pre-processed by applying the corrections prior to analysis by EV. The process could be streamlined by first editing large video files with the EV MASK editor prior to running the correction program. Note that lens corrections need to be applied to the *camera* calibration data as well as the raw flight data. See the **Camera Calibration** section in the text (pages 10-16).

REPORT DOCUMENTATION PAGE

Form Approved
OMB No. 0704-0188

1. AGENCY USE ONLY (Leave blank)	2. REPORT DATE	3. REPORT TYPE AND DATES COVERED
	September 1993	Corporate Report–Final

4. TITLE AND SUBTITLE

Flight Validation of a Pulsed Smoke Flow Visualization System

5. FUNDING NUMBERS

WU 533-02-35

6. AUTHOR(S)

Donald T. Ward and Kenneth M. Dorsett

7. PERFORMING ORGANIZATION NAME(S) AND ADDRESS(ES)

Aerospace Engineering Division
Texas Engineering Experiment Station
A & M University
College Station, Texas 77843-3141

8. PERFORMING ORGANIZATION REPORT NUMBER

H-1914
TEES-AERO-TR-93-1

9. SPONSORING/MONOTORING AGENCY NAME(S) AND ADDRESS(ES)

National Aeronautics and Space Administration
Washington, DC 20546-0001

10. SPONSORING/MONITORING AGENCY REPORT NUMBER

NASA CR-186026

11. SUPPLEMENTARY NOTES

Technical monitor for this project was John H. Del Frate, NASA Dryden Flight Research Facility, Edwards, California. This report was previously published as Texas A & M University report numbered TEES-AERO-TR 93-1, dated February 1993.

12a. DISTRIBUTION/AVAILABILITY STATEMENT

Unclassified—Unlimited
Subject Category 05

12b. DISTRIBUTION CODE

13. ABSTRACT (Maximum 200 words)

A flow visualization scheme, designed to measure vortex fluid dynamics on research aircraft, was validated in flight. Strake vortex trajectories and axial core velocities were determined using pulsed smoke, high-speed video images, and semiautomated image edge detection hardware and software. Smoke was pulsed by using a fast-acting three-way valve. After being redesigned because of repeatedly jamming in flight, the valve shuttle operated flawlessly during the last two tests. A 25-percent scale, Gothic strake was used to generate vortex over the wing of a GA-7 Cougar and was operated at a local angle of attack of 22° and Reynolds number of approximately 7.8×10^5/ft. Maximum axial velocities measured in the vortex core were between 1.75 and 1.95 times the freestream velocity. Analysis of the pulsed smoke system's affect on forebody vortices indicates that the system may reorient the forebody vortex system; however, blowing momentum coefficients normally used will have no appreciable affect on the leading-edge extension vortex system. It is recommended that a similar pulsed smoke system be installed on the F/A-18 High Angle Research Vehicle and that this approach be used to analyze vortex core dynamics during the remainder of its high-angle-of-attack research flights.

14. SUBJECT TERMS	15. NUMBER OF PAGES
Flight test, Flow visualization, Smoke pulsation, Vortex fluid dynamics	45
	16. PRICE CODE: A03

17. SECURITY CLASSIFICATION OF REPORT	18. SECURITY CLASSIFICATION OF THIS PAGE	19. SECURITY CLASSIFICATION OF ABSTRACT	20. LIMITATION OF ABSTRACT
Unclassified	Unclassified	Unclassified	Unlimited